Acta Mech 225, 2621–2643 (2014)
DOI 10.1007/s00707-014-1095-3

S. I. Kundalwal · M. C. Ray

Shear lag analysis of a novel short fuzzy fiber-reinforced composite

Received: 10 August 2013 / Revised: 22 December 2013 / Published online: 16 February 2014

Abstract A novel short fuzzy fiber-reinforced composite (SFFRC) in which the aligned short carbon fiber reinforcements are coated with radially aligned carbon nanotubes (CNTs) is considered in this study. A three-phase shear lag model considering radial and axial deformations of the different constituent phases of the SFFRC has been developed to analyze the stress transfer mechanisms of the SFFRC. Traditionally, the shear lag models have been developed with an application of the axial load only on the representative volume element (RVE) of the composite in an attempt for analyzing the stress transfer between the fiber and the matrix. The three-phase shear lag model derived in this study analyzes the stress transfer to the short carbon fiber considering the application of the axial as well as the radial loads on the RVE of the SFFRC. It is found that if the carbon fiber is coated with radially aligned CNTs, then the axial load transferred to the fiber is significantly reduced due to the radial stiffening of the polymer matrix by CNTs. When compared with the results without CNTs, it is found that almost ∼20 and ∼29 % reductions in the maximum axial stress in the carbon fiber and the interfacial shear stress along its length occur, respectively, if the value of the applied radial load is twice of the applied axial load and the value of the CNT volume fraction is 0.0236 in the SFFRC. Effects of the variation of the carbon fiber aspect ratio, the carbon fiber volume fraction, and the application of the radial load on the load transfer characteristics of the SFFRC are also investigated.

1 Introduction

The identification of carbon nanotubes (CNTs) [1] has stimulated a great deal of research concerning the prediction of their exceptionally high elastic properties [2–9]. The quest for utilizing such exceptional mechanical properties of CNTs and their high aspect ratio led to the opening of an emerging area of research on the development of CNT-reinforced composites [9–13]. To this end, the load transferred to the CNT reinforcements from the surrounding matrix is an important issue. A number of research studies have been carried out to investigate the load transfer characteristics of CNT-reinforced composites. For example, Schadler et al. [10] studied the mechanical behavior of multi-walled CNT-reinforced composites with both the tension and compression loading. They reported that the compression modulus is higher than that of the tensile modulus, indicating that the load transfer to CNTs in the nanocomposite is higher in compression. Li and Chou [11] developed a continuum-based numerical model for characterizing the interfacial shear stress between a CNT and the polymer matrix. Gao and Li [12] performed a shear lag analysis for the CNT-reinforced composite by replacing a CNT with an equivalent solid fiber. Their study reveals that the CNT aspect ratio significantly influences the stress transfer characteristics of the CNT-reinforced composite. An attempt has also been made by Jiang et al. [14] to characterize the non-bonded interface between a CNT and the polymer matrix through

S. I. Kundalwal · M. C. Ray (✉)
Department of Mechanical Engineering, Indian Institute of Technology, Kharagpur, 721302, India
E-mail: mcray@mech.iitkgp.ernet.in
Tel.: +91-322-2282984

the cohesive law. A micromechanical shear lag model has been developed by Li and Saigal [15] for assessing the interfacial shear stress transfer in CNT-reinforced polymer composites. Their results reveal that using sufficiently long and large CNTs, small CNT volume fraction improves the efficiency of the stress transfer in the CNT-reinforced composite. Zhang and He [16] theoretically investigated the viscoelastic behavior of CNT-reinforced composites by developing a three-phase shear lag model.

The manufacturing of unidirectional continuous CNT-reinforced composites in large scale has to encounter some challenging difficulties such as agglomeration of CNTs, misalignment, and difficulty in manufacturing very long CNTs. CNT-reinforced composites, developed so far, can improve the mechanical properties of the matrix and open a whole range of multifunctional applications for nanocomposite thin films. However, in terms of structural applications, these CNT-based composites cannot compete with traditional continuous fiber-reinforced composite materials. The combination of CNTs, polymer matrix, and advanced fibers to create so-called hybrid composites is seen as a practical approach to deriving structural/multifunctional benefits from CNTs. Further research on improving the out-of-plane properties of composites and better use of short CNTs led to the growth of CNTs on the surfaces of the advanced fibers. For example, Downs and Baker [17] reported the initial research work on the growth of carbon nanofibers on the surfaces of the commercial carbon fibers. They modified the surface area of the carbon fiber by coating with carbon nanofibers and found the significant enhancement in the adhesion properties at the fiber/matrix interface. Bower et al. [18] have grown aligned CNTs on the substrate surface using high-frequency microwave plasma-enhanced chemical vapor deposition with an extreme-case example of conformal radial growth of CNTs on the circumferential surface of a hair-thin optical fiber glass. They have found that the growth rate of CNTs is approximately 100 nm/s with entire growth of 12 μm and such CNT growth always occurs perpendicular to the substrate surface regardless of the substrate shape. The electrical self-bias imposed on the substrate surface was the primary mechanism responsible for CNTs alignment. Thostenson et al. [19] synthesized CNTs on the circumferential surfaces of the carbon fibers using chemical vapor deposition and found that the presence of CNTs at the fiber/matrix interface improves the interfacial shear strength of the composite. In their work, the surfaces of the carbon fibers after each step in the synthesization process of growing CNTs were examined with the scanning electron microscopy and found that no pitting was occurring on the carbon fiber surfaces. Zhao et al. [20] synthesized different morphologies of multi-walled CNTs on the circumferential surfaces of the carbon fibers by using floating catalyst method. Veedu et al. [21] demonstrated that the remarkable improvements in the interlaminar fracture toughness, hardness, delamination resistance, in-plane mechanical properties, damping, and thermoelastic behavior of the laminated composite can be obtained by growing about 60 μm-long multi-walled CNTs on the surfaces of the fibers. Electrophoresis technique was utilized for the selective deposition of CNTs on the surfaces of the carbon fibers by Bekyarova et al. [22]. For single-walled CNT (SWCNT)/carbon fiber-reinforced composite, they demonstrated ∼30 % enhancement in the interlaminar shear strength and twofold improvement of the out-of-plane electrical conductivity as compared to that of the composite without CNTs. Mathur et al. [23] experimentally demonstrated that the growth of CNTs on the carbon fibers causes excellent improvement in the mechanical properties of the carbon fiber-reinforced composite. They reported that the flexural strength is improved by 20 % for unidirectional, 75 % for 2D, and 66 % for 3D hybrid composites as compared to that of the composite with neat reinforcements. Growing CNTs on the woven carbon fiber, improved fracture toughness of the cured composite on the order of 50 % has been reported by Kepple et al. [24], while no loss in structural stiffness of the final composite structures is observed by them. Zhao et al. [25] investigated the effects of the surface morphology of carbon fibers and catalysts on the growth of CNTs on the circumferential surfaces of the carbon fibers. Tensile and compressive strengths of such hybrid nanocomposites have also been experimentally investigated in many research studies [22,26–29], and reported values of the strengths lie between 300 MPa and 1 GPa. A fiber coupled with radially grown CNTs on its circumferential surface is also being called as “fuzzy fiber” [30].

The extensive research on the growing of CNTs on the surfaces of the advanced fibers motivated the authors [31] to propose a novel short fuzzy fiber-reinforced composite (SFFRC) reinforced with zigzag CNTs and carbon fibers. The distinct constructional feature of such SFFRC is that the uniformly spaced CNTs are radially grown on the circumferential surfaces of the unidirectional short carbon fibers. They predicted that the transverse effective elastic properties of this novel SFFRC are significantly enhanced over their values without CNTs. To this end, the load transfer analysis of the SFFRC is yet to be investigated. Recently, Ray et al. [32] carried out a load transfer analysis of the short carbon fiber-reinforced composite in which the aligned CNTs are radially grown on the circumferential surfaces of the carbon fibers. In their study, the short carbon fibers being coated with radially grown CNTs were assumed to touch each other laterally, and, hence, a two-phase shear lag model was developed. In practice, the CNT-coated short carbon fibers may not touch each other laterally, and the corresponding representative volume element (RVE) for the shear lag analysis will be composed of three phases; namely, the carbon fiber, the CNT-reinforced polymer matrix composite, and the polymer matrix. However, a three-phase shear lag model of such SFFRC being composed of discontinuous fuzzy fiber reinforcements has not yet been derived. In this study, the authors intend to derive a closed-form three-phase shear lag model for analyzing the effect of radially grown CNTs on the load transferred to the short carbon fiber while the RVE is subjected to both axial and radial loads.

2 Shear lag model

The schematic diagrams illustrated in Fig. 1 represent a lamina of the SFFRC being studied here and its in-plane cross section. The novel constructional feature of such a composite is that uniformly aligned CNTs of equal length are radially grown on the circumferential surfaces of the short carbon fiber reinforcements. CNTs considered here are transversely isotropic [6,7,9]. They are grown on the circumferential surface of the carbon fiber in such a way that their axes of transverse isotropy are normal to the circumferential surface of the fiber. Such a resulting fuzzy fiber is shown in Fig. 2a. When this fuzzy fiber is embedded into the polymer material, the gaps between CNTs are filled up with the polymer, and the radially aligned CNTs eventually reinforce the polymer matrix surrounding the carbon fiber along the direction transverse to the length of the carbon fiber. Thus, the augmented fuzzy fiber can be viewed as a circular cylindrical short composite fuzzy fiber (SCFF) in which the carbon fiber is embedded in the CNT-reinforced polymer matrix nanocomposite (PMNC). This in turn allows one to treat the SFFRC as a composite in which the SCFFs are the reinforcements being embedded in the polymer matrix as shown in Fig. 2b. Figure 2b also illustrates a 3D structure of the RVE under consideration subjected to boundary conditions.

Figure 3 illustrates a cylindrical RVE based on which the three-phase shear lag model is derived. The cylindrical coordinate system (r, θ and x) is considered in such a way that the axis of the RVE coincides with

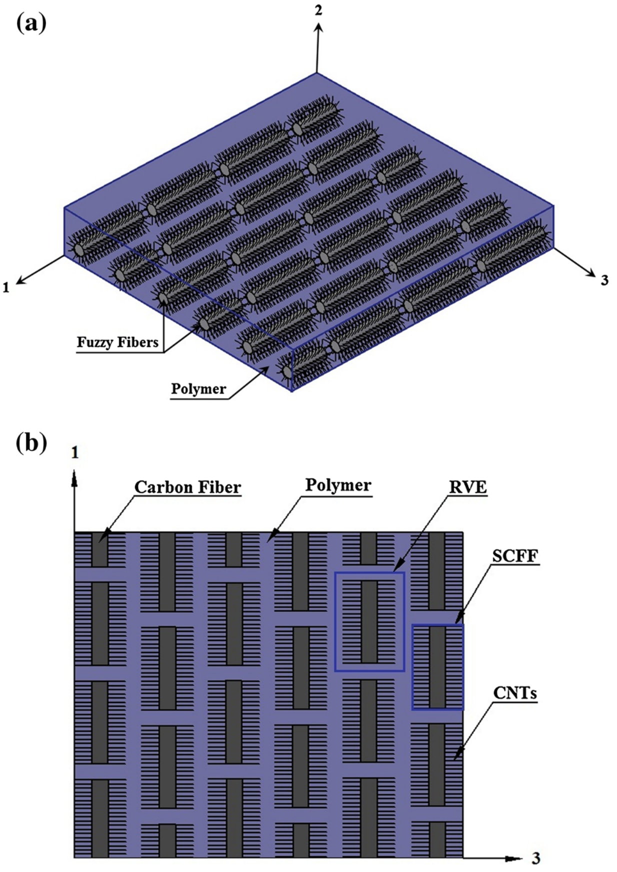

Fig. 1 **a** Schematic diagram of a lamina made of the SFFRC. **b** In-plane cross section of the SFFRC lamina

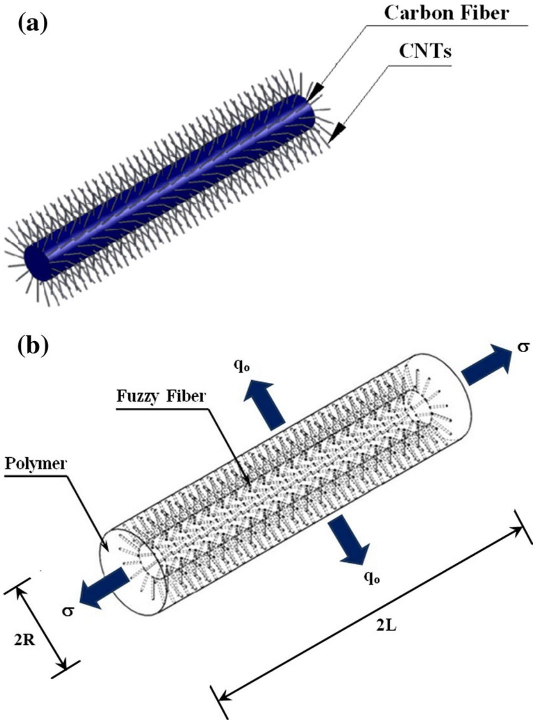

Fig. 2 **a** Fuzzy fiber with CNTs radially grown on its circumferential surface. **b** Load-carrying structure of the RVE of the SFFRC in which the SCFF is embedded in the polymer material

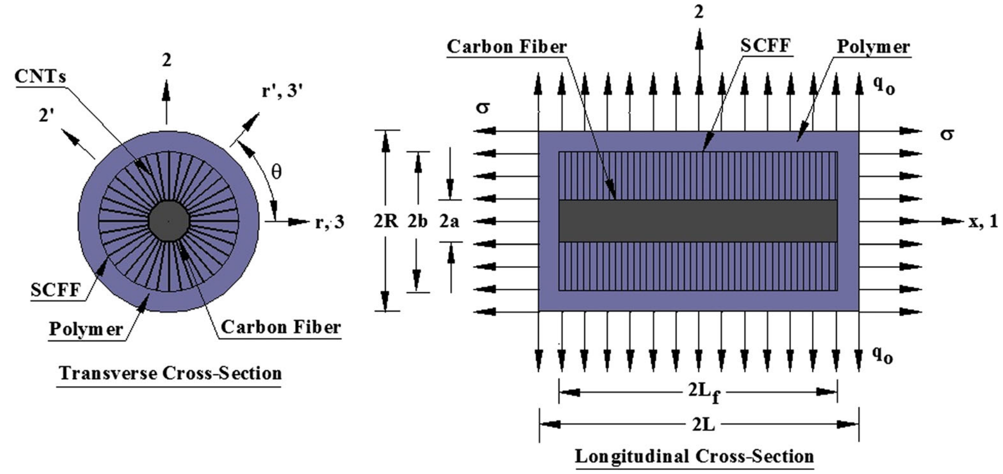

Fig. 3 Transverse and longitudinal cross sections of the three-phase RVE of the SFFRC

the *x*-axis while CNTs are aligned along the *r*-direction. The model is derived by dividing the RVE into three zones. The portion of the RVE in the zone $-L_f \leq x \leq L_f$ consists of three concentric cylindrical phases; namely, the carbon fiber, the PMNC, and the polymer matrix. The RVE of the SFFRC has the radius R and the length $2L$. The radius and the length of the carbon fiber are denoted by a and $2L_f$. The inner and outer radii of the PMNC phase are a and b, respectively. The portions of the RVE in the zones $-L \leq x \leq -L_f$ and $L_f \leq x \leq L$ are considered to be composed of an imaginary fiber, the imaginary PMNC, and the polymer matrix phase. The radius of the imaginary fiber is also denoted by a, while the inner and outer radii of the imaginary PMNC phase are also represented by a and b, respectively. Thus, the shear lag model derived for the zone $-L_f \leq x \leq L_f$ can be applied to derive the shear lag models for the zones $-L \leq x \leq -L_f$ and $L_f \leq x \leq L$. In what follows, the shear lag model for the zone $-L_f \leq x \leq L_f$ is first derived. As shown in Fig. 3, a tensile stress σ is applied to the RVE along the *x*-direction at $x = \pm L$ while the RVE is subjected to a radial normal stress q_o at $r = R$. In order to derive this shear lag model, the effective elastic properties of the PMNC phase are required. A three-phase Mori–Tanaka model is used to determine the effective elastic properties of the PMNC. The development of the Mori–Tanaka model is presented in "Appendix A." These results are used as an input to the shear lag model. Returning to the shear lag model, the governing equations for the different phases of the RVE concerning equilibrium along the x-direction are given by

$$\frac{\partial \sigma_x^i}{\partial x} + \frac{1}{r}\frac{\partial (r\sigma_{xr}^i)}{\partial r} = 0; \quad i = f, c \text{ and } m, \tag{1}$$

while the relevant constitutive relations are

$$\sigma_x^i = C_{11}^i \epsilon_x^i + C_{12}^i \epsilon_\theta^i + C_{13}^i \epsilon_r^i, \quad \sigma_r^i = C_{13}^i \epsilon_x^i + C_{23}^i \epsilon_\theta^i + C_{33}^i \epsilon_r^i \quad \text{and} \\ \sigma_{xr}^i = C_{66}^i \epsilon_{xr}^i; \quad i = f, c \quad \text{and } m. \tag{2}$$

In Eqs. (1) and (2), the superscripts *f*, *c*, and *m* denote, respectively, the carbon fiber, the PMNC, and the monolithic polymer matrix. For the *i*-th constituent phase, σ_x^i and σ_r^i represent the normal stresses in x and r directions, respectively; ϵ_x^i, ϵ_θ^i and ϵ_r^i are the normal strains along x, θ and r directions, respectively; σ_{xr}^i is the transverse shear stress, ϵ_{xr}^i is the transverse shear strain, and C_{ij}^i are the elastic constants. It should be noted here that the principle material coordinates axes (1–2–3) are coincident with the problem coordinate axes (x–θ–r). The strain–displacement relations for an axisymmetric problem relevant to this RVE are

$$\epsilon_x^i = \frac{\partial u^i}{\partial x}, \quad \epsilon_\theta^i = \frac{w^i}{r}, \quad \epsilon_r^i = \frac{\partial w^i}{\partial r} \quad \text{and} \quad \epsilon_{xr}^i = \frac{\partial u^i}{\partial r} + \frac{\partial w^i}{\partial x} \tag{3}$$

in which u^i and w^i represent the axial and the radial displacements at any point of the *i*-th phase along the x and the r direction, respectively. The traction boundary conditions are given by

$$\sigma_r^m\big|_{r=R} = q_o \quad \text{and} \quad \sigma_{xr}^m\big|_{r=R} = 0, \tag{4}$$

and the continuity conditions are

$$\sigma_r^f\Big|_{r=a} = \sigma_r^c\big|_{r=a}; \quad \sigma_{xr}^f\Big|_{r=a} = \sigma_{xr}^c\big|_{r=a} = \tau_i; \quad \sigma_r^c\big|_{r=b} = \sigma_r^m\big|_{r=b}; \quad \sigma_{xr}^c\big|_{r=b} = \sigma_{xr}^m\big|_{r=b} = \tau_o; \\ u^f\Big|_{r=a} = u^c\big|_{r=a}; \quad u^c\big|_{r=b} = u^m\big|_{r=b}; \quad w^f\Big|_{r=a} = w^c\big|_{r=a} \quad \text{and} \quad w^c\big|_{r=b} = w^m\big|_{r=b} \tag{5}$$

where τ_i is the transverse shear stress at the interface between the carbon fiber and the PMNC while τ_o is the transverse shear stress at the interface between the PMNC and the polymer matrix. The consideration of the radial load q_o on the RVE accounts for the lateral extensional interaction between the adjacent short carbon fibers. The average axial stresses in the different phases are defined as

$$\bar{\sigma}_x^f = \frac{1}{\pi a^2}\int_0^a \sigma_x^f 2\pi r \,\mathrm{d}r; \tag{6.1}$$

$$\bar{\sigma}_x^c = \frac{1}{\pi(b^2 - a^2)}\int_a^b \sigma_x^c 2\pi r \,\mathrm{d}r \quad \text{and} \quad \bar{\sigma}_x^m = \frac{1}{\pi(R^2 - b^2)}\int_b^R \sigma_x^m 2\pi r \,\mathrm{d}r. \tag{6.2,3}$$

Now, making use of Eqs. (1) and (4)–(6.1–3), it can be derived that

$$\frac{\partial \bar{\sigma}_x^f}{\partial x} = -\frac{2}{a}\tau_i; \quad \frac{\partial \bar{\sigma}_x^c}{\partial x} = \frac{2a}{b^2 - a^2}\tau_i - \frac{2b}{b^2 - a^2}\tau_o \quad \text{and} \quad \frac{\partial \bar{\sigma}_x^m}{\partial x} = \frac{2b}{R^2 - b^2}\tau_o, \tag{7.1–3}$$

It is evident from Eq. (7.1–3) that the gradients of $\bar{\sigma}_x^c$ and $\bar{\sigma}_x^m$ with respect to the axial coordinate (x) are independent of the radial coordinate (r). Hence, as the radial dimension of the RVE is very small, it is reasonable to assume that [33]

$$\frac{\partial \sigma_x^c}{\partial x} = \frac{\partial \bar{\sigma}_x^c}{\partial x} \quad \text{and} \quad \frac{\partial \sigma_x^m}{\partial x} = \frac{\partial \bar{\sigma}_x^m}{\partial x}. \tag{8}$$

Thus, using the equilibrium equation given by Eq. (1), the transverse shear stresses in the PMNC phase and in the polymer matrix phase can be expressed in terms of the interfacial shear stresses τ_i and τ_o, respectively, as follows:

$$\sigma_{xr}^{c} = \frac{a}{r}\tau_i + \frac{1}{2r}\left(a^2 - r^2\right)\frac{\partial \bar{\sigma}_x^{c}}{\partial x}, \tag{9}$$

$$\sigma_{xr}^{m} = \left(\frac{R^2}{r} - r\right)\frac{b}{R^2 - b^2}\tau_o. \tag{10}$$

Also, since the RVE is an axisymmetric problem, it is usually assumed [33] that the gradient of the radial displacements with respect to the x-direction is negligible, and so, from the constitutive relation given by Eq. (2) and the strain–displacement relations given by Eq. (3) between σ_{xr}^{i} and ϵ_{xr}^{i}, one can write

$$\frac{\partial u^c}{\partial r} = \frac{1}{C_{66}^{c}}\sigma_{xr}^{c} \quad \text{and} \quad \frac{\partial u^m}{\partial r} = \frac{1}{C_{66}^{m}}\sigma_{xr}^{m}. \tag{11}$$

Solving Eq. (11) and satisfying the continuity condition at $r = a$ and $r = b$, respectively, the axial displacements of the PMNC phase and the polymer matrix phase along the x-direction can be derived as follows:

$$u^c = u_a^f + A_1\tau_i + A_2\tau_o, \tag{12}$$

$$u^m = u_a^f + A_3\tau_i + A_4\tau_o \quad \text{and} \tag{13}$$

$$u_a^f = u^f\Big|_{r=a} \tag{14}$$

in which A_i ($i = 1, 2, 3,$ and 4) are the constants of the displacement fields of the PMNC and the polymer matrix and are explicitly shown in “Appendix B.”

The radial displacements in the three constituent phases can be assumed as [34]

$$w^f = A_f r, \quad w^c = A_c r + \frac{B_c}{r} \quad \text{and} \quad w^m = A_m r + \frac{B_m}{r} \tag{15}$$

where $A_f,\ A_c,\ B_c,\ A_m$ and B_m are unknown constants. Invoking the continuity conditions for the radial displacement at the interfaces $r = a$ and b, the radial displacement in the PMNC phase can be augmented as

$$w^c = \frac{a^2}{b^2 - a^2}\left(\frac{b^2}{r} - r\right)A_f - \frac{b^2}{b^2 - a^2}\left(\frac{a^2}{r} - r\right)A_m - \frac{1}{b^2 - a^2}\left(\frac{a^2}{r} - r\right)B_m. \tag{16}$$

Substituting Eqs. (12), (13), (15), and (16) into Eq. (3) and subsequently, employing the constitutive relations (2), the expressions for the normal stresses can be written in terms of the unknowns $A_f,\ A_m$ and B_m as follows:

$$\bar{\sigma}_x^{f} = C_{11}^{f}\frac{\partial u_a^f}{\partial x} + 2C_{12}^{f}A_f, \tag{17}$$

$$\sigma_r^{f} = \frac{C_{12}^{f}}{C_{11}^{f}}\bar{\sigma}_x^{f} + \left[C_{23}^{f} + C_{33}^{f} - \frac{2\left(C_{12}^{f}\right)^2}{C_{11}^{f}}\right]A_f, \tag{18}$$

$$\begin{aligned}\sigma_x^{c} = {} & \frac{C_{11}^{c}}{C_{11}^{f}}\bar{\sigma}_x^{f} - \left(\frac{2C_{12}^{c}a^2}{b^2 - a^2} + \frac{2C_{12}^{f}C_{11}^{c}}{C_{11}^{f}}\right)A_f + \frac{2C_{12}^{c}b^2}{b^2 - a^2}A_m + \frac{2C_{12}^{c}}{b^2 - a^2}B_m + C_{11}^{c}A_1\frac{\partial \tau_i}{\partial x} \\ & + C_{11}^{c}A_2\frac{\partial \tau_o}{\partial x},\end{aligned} \tag{19}$$

$$\begin{aligned}\sigma_r^{c} = {} & \frac{C_{13}^{c}}{C_{11}^{f}}\bar{\sigma}_x^{f} + \left[C_{13}^{c}\frac{a^2}{b^2 - a^2}\left(\frac{b^2}{r^2} - 1\right) + C_{33}^{c}\frac{a^2}{b^2 - a^2}\left(-\frac{b^2}{r^2} - 1\right) - \frac{2C_{12}^{f}C_{13}^{c}}{C_{11}^{f}}\right]A_f \\ & + \left[-C_{13}^{c}\frac{b^2}{b^2 - a^2}\left(\frac{a^2}{r^2} - 1\right) + C_{33}^{c}\frac{b^2}{b^2 - a^2}\left(\frac{a^2}{r^2} + 1\right)\right]A_m\end{aligned}$$

$$+\left[-C_{23}^{c}\frac{1}{b^2-a^2}\left(\frac{a^2}{r^2}-1\right)+C_{33}^{c}\frac{1}{b^2-a^2}\left(\frac{a^2}{r^2}+1\right)\right]B_m+C_{13}^{c}A_1\frac{\partial\tau_i}{\partial x}+C_{13}^{c}A_2\frac{\partial\tau_o}{\partial x}, \tag{20}$$

$$\sigma_x^m=\frac{C_{11}^m}{C_{11}^f}\bar{\sigma}_x^f-\frac{2C_{12}^fC_{11}^m}{C_{11}^f}A_f+2C_{12}^mA_m+C_{11}^mA_3\frac{\partial\tau_i}{\partial x}+C_{11}^mA_4\frac{\partial\tau_o}{\partial x}, \tag{21}$$

$$\sigma_r^m=\frac{C_{12}^m}{C_{11}^f}\bar{\sigma}_x^f-\frac{2C_{12}^fC_{12}^m}{C_{11}^f}A_f+\left(C_{11}^m+C_{12}^m\right)A_m+\left(C_{12}^m-C_{11}^m\right)\frac{B_m}{r^2}+C_{12}^mA_3\frac{\partial\tau_i}{\partial x}$$
$$+C_{12}^mA_4\frac{\partial\tau_o}{\partial x}. \tag{22}$$

Invoking the continuity conditions $\left.\sigma_r^f\right|_{r=a}=\left.\sigma_r^c\right|_{r=a}$ and $\left.\sigma_r^c\right|_{r=b}=\left.\sigma_r^m\right|_{r=b}$, and satisfying the boundary condition $\left.\sigma_r^m\right|_{r=R}=q_o$, the following equations for solving $A_f,\ A_m$ and B_m are obtained:

$$\begin{bmatrix}A_{11}&A_{12}&A_{13}\\A_{21}&A_{22}&A_{23}\\A_{31}&A_{32}&A_{33}\end{bmatrix}\begin{Bmatrix}A_f\\A_m\\B_m\end{Bmatrix}=\frac{\bar{\sigma}_x^f}{C_{11}^f}\begin{Bmatrix}C_{12}^f-C_{13}^c\\C_{13}^c-C_{12}^m\\-C_{12}^m\end{Bmatrix}+\begin{Bmatrix}-C_{13}^cA_1\\C_{13}^cA_1-C_{12}^mA_3\\-C_{12}^mA_3\end{Bmatrix}\frac{\partial\tau_i}{\partial x}$$
$$+\begin{Bmatrix}-C_{13}^cA_2\\(C_{13}^cA_2-C_{12}^mA_4)\\-C_{12}^mA_6\end{Bmatrix}\frac{\partial\tau_o}{\partial x}+\begin{Bmatrix}0\\0\\1\end{Bmatrix}q_o. \tag{23}$$

Solving Eq. (23), the solutions of the constants of the radial displacements $A_f,\ A_m$ and B_m can be expressed as follows:

$$A_f=k_{11}\bar{\sigma}_x^f+k_{12}\frac{\partial\tau_i}{\partial x}+k_{13}\frac{\partial\tau_o}{\partial x}+k_{14}q_o,$$
$$A_m=k_{21}\bar{\sigma}_x^f+k_{22}\frac{\partial\tau_i}{\partial x}+k_{23}\frac{\partial\tau_o}{\partial x}+k_{24}q_o,$$
$$B_m=k_{31}\bar{\sigma}_x^f+k_{32}\frac{\partial\tau_i}{\partial x}+k_{33}\frac{\partial\tau_o}{\partial x}+k_{34}q_o. \tag{24}$$

The expressions of the coefficients A_{ij} are presented in "Appendix B." The expressions of the coefficients k_{ij} are evident from Eqs. (23) and (24) and are not shown here for the sake of brevity.

Now, making use of Eqs. (19), (21), and (24) in Eqs. (6.2,3), the average axial stresses in the PMNC phase and the polymer matrix phase are written as follows:

$$\bar{\sigma}_x^c=L_1\bar{\sigma}_x^f+L_2\frac{\partial\tau_i}{\partial x}+L_3\frac{\partial\tau_o}{\partial x}+L_4q_o, \tag{25}$$
$$\bar{\sigma}_x^m=L_5\bar{\sigma}_x^f+L_6\frac{\partial\tau_i}{\partial x}+L_7\frac{\partial\tau_o}{\partial x}+L_8q_o. \tag{26}$$

The constants L_i (i = 1, 2, 3, …, 8) appearing in the above two equations are presented in "Appendix B."

Now, satisfying the equilibrium of force along the axial (x) direction at any transverse cross section of the RVE, the following equation is obtained:

$$\pi R^2\sigma=\pi\left(R^2-b^2\right)\bar{\sigma}_x^m+\pi\left(b^2-a^2\right)\bar{\sigma}_x^c+\pi a^2\bar{\sigma}_x^f. \tag{27}$$

Differentiating Eq. (7.1) and (7.3) with respect to x, we have

$$\frac{\partial\tau_i}{\partial x}=-\frac{a}{2}\frac{\partial^2\bar{\sigma}_x^f}{\partial x^2}, \tag{28}$$
$$\frac{\partial\tau_o}{\partial x}=\frac{R^2-b^2}{2b}\frac{\partial^2\bar{\sigma}_x^m}{\partial x^2}. \tag{29}$$

Use of Eqs. (25), (26), (27)–(29) yields

$$L_9\bar{\sigma}_x^f + L_{10}\frac{\partial^2\bar{\sigma}_x^f}{\partial x^2} + L_{11}\frac{\partial^2\bar{\sigma}_x^m}{\partial x^2} + L_{12}q_o - R^2\sigma = 0 \tag{30}$$

where

$$L_9 = a^2 + \left(b^2 - a^2\right)L_1 + \left(R^2 - b^2\right)L_5, \quad L_{10} = -(a/2)\left[\left(b^2 - a^2\right)L_2 + \left(R^2 - b^2\right)L_6\right],$$
$$L_{11} = \left(\frac{R^2 - b^2}{2b}\right)\left[\left(b^2 - a^2\right)L_3 + \left(R^2 - b^2\right)L_7\right] \quad \text{and} \quad L_{12} = \left(b^2 - a^2\right)L_4 + \left(R^2 - b^2\right)L_8,$$

Deriving the expression for $\frac{\partial\tau_o}{\partial x}$ from Eq. (25) and substituting the same into Eq. (26) and then using Eq. (28), the following result for $\bar{\sigma}_x^m$ is obtained:

$$\bar{\sigma}_x^m = \left(L_5 - \frac{L_1L_7}{L_3}\right)\bar{\sigma}_x^f + \left(\frac{L_7}{L_3}\right)\bar{\sigma}_x^c + \left(\frac{a}{2}\right)\left(\frac{L_2L_7}{L_3} - L_6\right)\frac{\partial^2\bar{\sigma}_x^f}{\partial x^2} + \left(L_8 - \frac{L_4L_7}{L_3}\right)q_o, \tag{31}$$

Differentiating Eqs. (27) and (31) twice with respect to x and using the resulting equations in Eq. (30), the governing equation for the average axial stress in the carbon fiber coated with radially grown aligned CNTs is obtained as follows:

$$\frac{\partial^4\bar{\sigma}_x^f}{\partial x^4} + L_{14}\frac{\partial^2\bar{\sigma}_x^f}{\partial x^2} + L_{15}\bar{\sigma}_x^f - L_{16}\sigma + L_{17}q_o = 0. \tag{32}$$

The coefficients L_i (i=14, 15, 16 and 17) appearing in the above differential equation have been explicitly presented in "Appendix B."

Following the above procedure, the governing equation for the average axial stress ($\bar{\sigma}_x^{pf}$) in the imaginary fiber made of the polymer material lying in the zones $-L \le x \le -L_f$ and $L_f \le x \le L$ can be written as follows:

$$\frac{\partial^4\bar{\sigma}_x^{pf}}{\partial x^4} + L_{14}^{pf}\frac{\partial^2\bar{\sigma}_x^{pf}}{\partial x^2} + L_{15}^{pf}\bar{\sigma}_x^{pf} - L_{16}^{pf}\sigma + L_{17}^{pf}q_o = 0. \tag{33}$$

In the above equation, the expressions for L_{14}^{pf}, L_{15}^{pf}, L_{16}^{pf}, and L_{17}^{pf} are similar to those of the expressions L_{14}, L_{15}, L_{16}, and L_{17}, respectively. But these are to be derived by considering $C_{ij}^f = C_{ij}^c = C_{ij}^m$. Solutions of Eqs. (32) and (33) are given by:

$$\begin{aligned}\bar{\sigma}_x^f &= (L_{16}/L_{15})\sigma - (L_{17}/L_{15})q_o + L_{18}\sinh(\beta x) + L_{19}\cosh(\beta x) + L_{20}\sinh(\alpha x)\\ &\quad + L_{21}\cosh(\alpha x), \qquad (34)\\ \bar{\sigma}_x^{pf} &= \left(L_{16}^{pf}/L_{15}^{pf}\right)\sigma - \left(L_{17}^{pf}/L_{15}^{pf}\right)q_o + L_{18}^{pf}\sinh\left(\beta^{pf}x\right) + L_{19}^{pf}\cosh\left(\beta^{pf}x\right) + L_{20}^{pf}\sinh\left(\alpha^{pf}x\right)\\ &\quad + L_{21}^{pf}\cosh\left(\alpha^{pf}x\right) \qquad (35)\end{aligned}$$

where

$$\beta = \sqrt{1/2\left(-L_{14} + \sqrt{(L_{14})^2 - 4L_{15}}\right)}, \quad \alpha = \sqrt{1/2\left(-L_{14} - \sqrt{(L_{14})^2 - 4L_{15}}\right)},$$
$$\beta^{pf} = \sqrt{1/2\left(-L_{14}^{pf} + \sqrt{\left(L_{14}^{pf}\right)^2 - 4L_{15}^{pf}}\right)} \quad \text{and} \quad \alpha^{pf} = \sqrt{1/2\left(-L_{14}^{pf} - \sqrt{\left(L_{14}^{pf}\right)^2 - 4L_{15}^{pf}}\right)}. \tag{36}$$

The constants L_{18}, L_{18}^{pf}, L_{19}, L_{19}^{pf}, L_{20}, L_{20}^{pf}, L_{21}, and L_{21}^{pf} are to be evaluated from the following end conditions:

$$\bar{\sigma}_x^{pf} = \sigma \quad \text{at } x = \pm L \quad \text{and} \quad \frac{\partial\bar{\sigma}_x^{pf}}{\partial x} = 0 \quad \text{at } x = \pm L, \tag{37}$$

$$\bar{\sigma}_x^f = \bar{\sigma}_x^{pf} \quad \text{at } x = \pm L_f \quad \text{and} \quad \frac{\partial\bar{\sigma}_x^f}{\partial x} = \frac{\partial\bar{\sigma}_x^{pf}}{\partial x} \quad \text{at } x = \pm L_f. \tag{38}$$

Utilizing the end conditions given by Eq. (37) in Eq. (35), the constants L_{18}^{pf}, L_{19}^{pf}, L_{20}^{pf} and L_{21}^{pf} can be explicitly expressed as follows:

$$L_{18}^{pf} = 0, \tag{39}$$

$$\begin{aligned} L_{19}^{pf} &= -\frac{\alpha^{pf} \sinh\left(\alpha^{pf} L\right)}{\alpha^{pf} \sinh\left(\alpha^{pf} L\right) \cosh\left(\beta^{pf} L\right) - \beta^{pf} \sinh\left(\beta^{pf} L\right) \cosh\left(\alpha^{pf} L\right)}, \\ &\quad \times \left\{ \frac{L_{16}^{pf}}{L_{15}^{pf}} \sigma - \frac{L_{17}^{pf}}{L_{15}^{pf}} q_o - \sigma \right\}, \end{aligned} \tag{40}$$

$$L_{20}^{pf} = 0, \tag{41}$$

$$\begin{aligned} L_{21}^{pf} &= \frac{\beta^{pf} \sinh\left(\beta^{pf} L\right)}{\alpha^{pf} \sinh\left(\alpha^{pf} L\right) \cosh\left(\beta^{pf} L\right) - \beta^{pf} \sinh\left(\beta^{pf} L\right) \cosh\left(\alpha^{pf} L\right)} \\ &\quad \times \left\{ \frac{L_{16}^{pf}}{L_{15}^{pf}} \sigma - \frac{L_{17}^{pf}}{L_{15}^{pf}} q_o - \sigma \right\}. \end{aligned} \tag{42}$$

Substituting Eqs. (39)–(42) in Eq. (35), the final solution for $\bar{\sigma}_x^{pf}$ is obtained as follows:

$$\begin{aligned} \bar{\sigma}_x^{pf} &= \left[\frac{\beta^{pf} \sinh\left(\beta^{pf} L\right) \cosh\left(\alpha^{pf} x\right) - \alpha^{pf} \sinh\left(\alpha^{pf} L\right) \cosh\left(\beta^{pf} x\right)}{\alpha^{pf} \sinh\left(\alpha^{pf} L\right) \cosh\left(\beta^{pf} L\right) - \beta^{pf} \sinh\left(\beta^{pf} L\right) \cosh\left(\alpha^{pf} L\right)} \right] \\ &\quad \times \left\{ \frac{L_{16}^{pf}}{L_{15}^{pf}} \sigma - \frac{L_{17}^{pf}}{L_{15}^{pf}} q_o - \sigma \right\} + \frac{L_{16}^{pf}}{L_{15}^{pf}} \sigma - \frac{L_{17}^{pf}}{L_{15}^{pf}} q_o. \end{aligned} \tag{43}$$

Similarly, utilizing the end conditions given by Eq. (38) in Eq. (34), the constants L_{18}, L_{19}, L_{20}, and L_{21} are evaluated, and the same have been explicitly shown in "Appendix B." Substitution of Eq. (34) into Eq (7.1) yields the expression for the carbon fiber/PMNC interfacial shear stress as follows:

$$\tau_i = -\frac{a}{2} \left[\beta L_{18} \cosh(\beta x) + \beta L_{19} \sinh(\beta x) + \alpha L_{20} \cosh(\alpha x) + \alpha L_{21} \sinh(\alpha x) \right]. \tag{44}$$

Following the procedure for deriving the solutions of the average axial stresses $\bar{\sigma}_x^{f}$ and $\bar{\sigma}_x^{pf}$ in the carbon fiber and the imaginary fiber, respectively, the solutions for the average axial stresses $\bar{\sigma}_x^{m}$ and $\bar{\sigma}_x^{pm}$ in the polymer matrices surrounding the SCFF and the imaginary SCFF, respectively, can be derived as follows:

$$\begin{aligned} \bar{\sigma}_x^{m} &= \left(L_{30}/L_{29}\right) \sigma - \left(L_{31}/L_{29}\right) q_o + L_{32} \sinh\left(\beta^{m} x\right) + L_{33} \cosh\left(\beta^{m} x\right) + L_{34} \sinh\left(\alpha^{m} x\right) \\ &\quad + L_{35} \cosh\left(\alpha^{m} x\right), \end{aligned} \tag{45}$$

$$\begin{aligned} \bar{\sigma}_x^{pm} &= \left(L_{30}^{pm}/L_{29}^{pm}\right) \sigma - \left(L_{31}^{pm}/L_{29}^{pm}\right) q_o + L_{32}^{pm} \sinh\left(\beta^{pm} x\right) + L_{33}^{pm} \cosh\left(\beta^{pm} x\right) + L_{34}^{pm} \sinh\left(\alpha^{pm} x\right) \\ &\quad + L_{35}^{pm} \cosh\left(\alpha^{pm} x\right) \end{aligned} \tag{46}$$

where

$$\begin{aligned} \beta^{m} &= \sqrt{1/2 \left(-L_{28} + \sqrt{\left(L_{28}\right)^2 - 4 L_{29}} \right)}, \quad \alpha^{m} = \sqrt{1/2 \left(-L_{28} - \sqrt{\left(L_{28}\right)^2 - 4 L_{29}} \right)}, \\ \beta^{pm} &= \sqrt{1/2 \left(-L_{28}^{pm} + \sqrt{\left(L_{28}^{pm}\right)^2 - 4 L_{29}^{pf}} \right)} \text{ and } \alpha^{pm} = \sqrt{1/2 \left(-L_{28}^{pm} - \sqrt{\left(L_{28}^{pm}\right)^2 - 4 L_{29}^{pm}} \right)}. \end{aligned} \tag{47}$$

The constants L_{32}, L_{32}^{pm}, L_{33}, L_{33}^{pm}, L_{34}, L_{34}^{pm}, L_{35}, and L_{35}^{pm} are to be evaluated from the boundary conditions given in Eqs. (37) and (38). Also, the coefficients $(L_{28}) - (L_{31})$ appearing in Eqs. (45)–(47) are presented in "Appendix B." Finally, substitution of Eq. (45) into Eq. (7.3) yields the expression for the SCFF/polymer matrix interfacial shear stress as follows:

$$\tau_o = \left(\frac{R^2 - b^2}{b^2 - a^2}\right)\left[\beta^m L_{32}\cosh\left(\beta^m x\right) + \beta^m L_{33}\sinh\left(\beta^m x\right) + \alpha^m L_{34}\cosh\left(\alpha^m x\right) + \alpha^m L_{35}\sinh\left(\alpha^m x\right)\right]. \tag{48}$$

3 Results and discussion

Zigzag CNTs, carbon fiber, and polyimide matrix are used for evaluating the numerical results. Their material properties are taken from references [9,35,36] and are listed in Table 1. The effective elastic properties and the thickness of the hollow circular cylindrical continuum representing the interphase between a CNT and the polyimide matrix are also presented in Table 1. Unless otherwise mentioned, the values of the geometrical parameters of the RVE of the SFFRC are taken as follows:

$$2a = 10\,\mu\text{m}, \quad L_f/a = 20, \quad L/L_f = 1.1 \quad \text{and} \quad D/D_b = 1.1$$

where a, L, L_f, D, and D_b represent carbon fiber radius, half length of the RVE, half length of the SCFF, diameter of the RVE, and diameter of the SCFF, respectively. Volume fraction of the CNT (V_{CNT}) in the SFFRC depends on the CNT diameter, the carbon fiber diameter, and the surface-to-surface distance between two adjacent radially aligned CNTs at their roots. In the absence of any interphase between CNTs, it is reported [37] that the minimum surface-to-surface distance between two adjacent CNTs is the equilibrium van der Waals distance, which is about 0.34 nm. Since in the PMNC material, polymer molecules fill the gaps between CNTs and the formation of the interphase is also considered between a CNT and the polymer, the surface-to-surface distance between two adjacent CNTs at their roots is considered as 1.7 nm. In the SFFRC, the hexagonal packing array of SCFFs is considered as shown in Fig. 4 for evaluating the numerical results while they are not touching each other.

The determination of V_{CNT} in the SFFRC is an important issue. It is obvious that the constructional feature of the SFFRC imposes a constraint on the maximum value of V_{CNT}. Based on the surface-to-surface distance

Table 1 Material properties of the constituent phases of the SFFRC

Material	Reference	C_{11} (GPa)	C_{12} (GPa)	C_{13} (GPa)	C_{23} (GPa)	C_{33} (GPa)	C_{44} (GPa)	C_{66} (GPa)	(nm)
(10, 0) CNT	[9]	709.9	172.4	240	240	1,513.1	1,120	268.7	$d_n = 0.78$
Interphase		29.6	15.2	15.2	15.2	29.6	7.2	7.2	Gap = 0.3333
(14, 0) CNT	[9]	557.5	137.5	187.7	187.7	1,082.8	779.2	210	$d_n = 1.1$
Interphase		27.63	14.23	14.23	14.23	27.63	6.70	6.70	Gap = 0.3236
(18, 0) CNT	[9]	472.9	118.7	159.7	159.7	846.1	596.3	177.1	$d_n = 1.42$
Interphase		27.55	14.19	14.19	14.19	27.55	6.68	6.68	Gap = 0.3158
Carbon fiber	[35]	236.4	10.6	10.6	10.7	24.8	7	25	d = 10,000
Polyimide	[36]	9	6	6	6	9	1.5	1.5	–

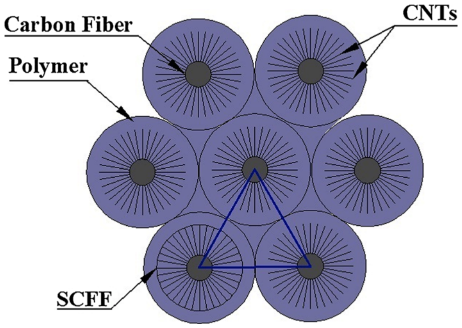

Fig. 4 Hexagonal packing array comprised of SCFFs dispersed in the polymer matrix

Table 2 Effective elastic coefficients of the PMNC

CNT Type	D/D_b & L/L_f	v_f	$(v_n)_\mathrm{max}$	C^c_{11} (GPa)	C^c_{12} (GPa)	C^c_{23} (GPa)	C^c_{33} (GPa)	C^c_{44} (GPa)	C^c_{66} (GPa)
(10, 0)	1.1	0.3	0.062	11.266	7.108	17.609	43.740	13.066	2.426
(14, 0)	1.1	0.3	0.097	11.789	7.347	18.816	47.483	14.333	2.669
(18, 0)	1.1	0.3	0.130	12.344	7.610	19.369	49.250	14.941	2.929
(10, 0)	1.2	0.3	0.067	11.484	7.214	18.543	46.528	13.993	2.513
(10, 0)	1.3	0.3	0.072	11.695	7.316	19.419	49.143	14.862	2.596
(10, 0)	1.4	0.3	0.076	11.898	7.414	20.239	51.591	15.676	2.676
(10, 0)	1.1	0.1	0.043	10.484	6.727	14.034	33.057	9.511	2.112
(10, 0)	1.1	0.2	0.055	10.950	6.954	16.213	39.571	11.679	2.3
(10, 0)	1.1	0.4	0.067	11.507	7.225	18.639	46.816	14.089	2.522
(10, 0)	1.1	0.5	0.072	11.704	7.320	19.454	49.249	14.897	2.6

at the roots of two adjacent CNTs and the CNT diameter, the maximum number of CNTs grown on the circumferential surface of a carbon fiber of particular diameter can be determined. Then, based on the carbon fiber volume fraction (v_f) in the SFFRC, the maximum value of V_CNT can be determined as [31]

$$(V_\mathrm{CNT})_\mathrm{max} = \frac{V^\mathrm{CNT}}{V^\mathrm{FFRC}} = \frac{\pi d_n^2}{2\,(d_n + 1.7)^2}\left(\frac{b}{a} - 1\right) v_\mathrm{f}. \tag{49}$$

where d_n is the diameter of the CNT. First, the effective elastic coefficients of the PMNC are computed by employing the three-phase Mori–Tanaka method. Estimated values of the effective elastic coefficients of the PMNC are summarized in Table 2. It may be noted that as the integer for designating the zigzag CNT increases, the diameter of the CNT increases. These results reveal that if the CNT diameter is varied till that of (18, 0) CNT, then the increase in the CNT diameter marginally enhances the values of the effective elastic coefficients of the PMNC. This may be attributed to the fact that as the CNT diameter increases, the value of the CNT volume fraction increases, which results in the increase in the values of the effective elastic coefficients of the PMNC. In many research studies, tensile and compressive strengths of the hybrid nanocomposites have been experimentally investigated, and reported values of the strengths lie between 300 MPa and 1 GPa [22,26–29]. However, the study concerned with the investigation of the strengths of the SFFRC is not yet reported in the literature. Hence, the applied axial and radial loads on the RVE are normalized in the present study. For analyzing the stress transfer characteristics of the SFFRC, the following non-dimensional parameters are used:

$$\sigma^* = \frac{\bar{\sigma}_x^f}{\sigma}, \quad \tau^* = \frac{\tau_i}{\sigma} \quad \text{and} \quad \tau_o^* = \frac{\tau_o}{\sigma}. \tag{50}$$

In order to validate the three-phase shear lag model derived in Sect. 2, first the normalized average axial stress (σ^*) in the CNT fiber and the interfacial shear stress (τ^*) along its length computed by the present model are compared with those obtained by an existing model [15]. For such comparison, material properties of the (20, 0) CNT and the polymer matrix are taken as $E^n = 1{,}034\,\mathrm{GPa}$, $\mu^n = 0.28$, $E^p = 2.41$ GPa and $\mu^p = 0.35$ as considered by Li and Saigal [15]. For the CNT aspect ratio 50 and the CNT volume fraction 0.1, the comparisons of the average axial stress in the CNT fiber and the interfacial shear stress along its length computed by the present model and the model by Li and Saigal [15] are presented in Fig. 5a, b, respectively. It may be noted that the good agreement between the two sets of results has been obtained verifying the present shear lag model. The marginal differences observed may be attributed to the fact that the shear lag model of Li and Saigal [15] did not consider the radial deformations in the constituent phases of the composite, whereas in the present shear lag model, the radial deformations of the different constituent phases of the composite have been taken into account.

The main novelty of the three-phase shear lag model derived in this study is that the radial deformations of the transversely isotropic constituent phases (i.e., the CNT, the carbon fiber, and the PMNC) of the SFFRC and the application of the radial load on the RVE of the SFFRC have been taken into account, which have not been considered in the existing shear lag studies. However, it is imperative to justify the validity of the shear lag model derived in Sect. 2 considering the different transversely isotropic constituent phases of the SFFRC and the application of the radial load on the RVE. For this purpose, three-phase finite element (FE) shear lag models have been developed using the commercial software ANSYS 11.0 to validate the analytical shear lag model derived in Sect. 2. The finite element model of the three-phase RVE of the SFFRC has been shown in Fig. 6. It should be noted that, because of the symmetry, one-half of the RVE is considered for the FE

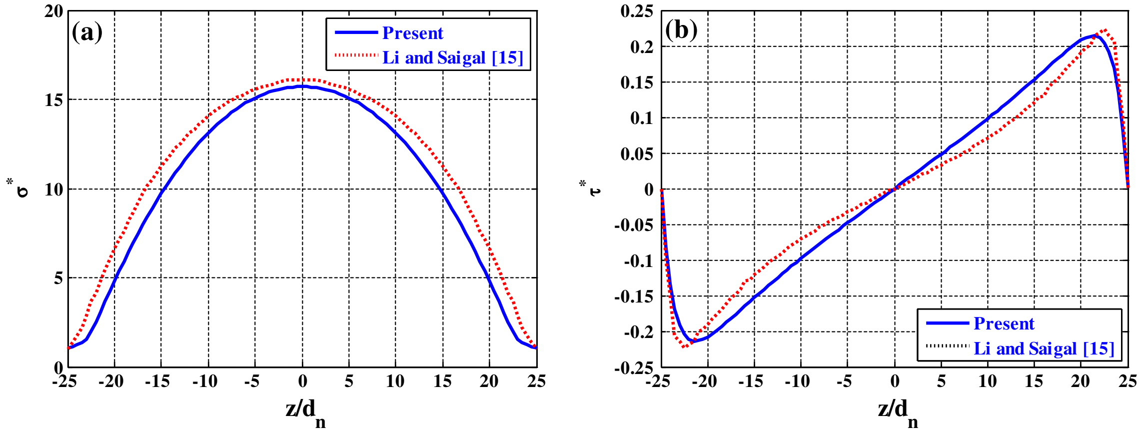

Fig. 5 Comparisons of **a** the average axial stress and **b** the interfacial shear stress along the length of the CNT fiber computed by the present shear lag model with those predicted by the shear lag model by Li and Saigal [15]

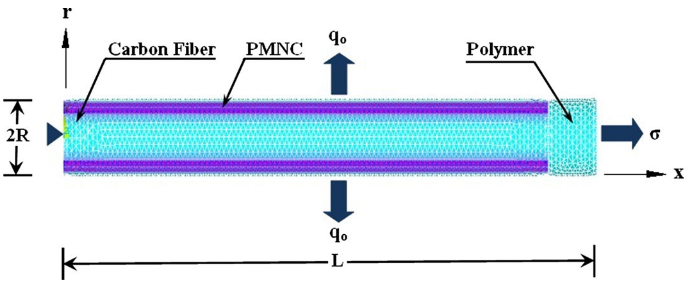

Fig. 6 FE mesh of the RVE of the SFFRC

simulations. Under the conditions of an imposed tensile stress (σ) and radial normal stress (q_o) on the RVE of the SFFRC, the average stresses $\left\{\bar{\sigma}^i\right\}$ in the i-th phase of the RVE can be obtained as follows:

$$\left\{\bar{\sigma}^i\right\} = \frac{1}{V^i}\int \left\{\sigma^i\right\} \mathrm{d}V^i; \quad i = f, c \text{ and } m \tag{51}$$

where V^i represents the volume of the i-th phase of the RVE, and the field variable with an overbar represents the average of the field variable. As shown in Fig. 6, a tensile stress σ is applied to the RVE along the x-direction at $x = L$, while the RVE is subjected to a radial normal stress q_o at $r = R$ and its one end is constrained at $x = 0$. With and without the application of the radial normal stress (q_o), the comparisons of the average axial stress in the carbon fiber and the interfacial shear stress between the carbon fiber and the PMNC computed by the analytical shear lag model and the FE shear lag model are presented in Fig. 7a, b, respectively. It may be observed that the excellent agreement between the two sets of results has been obtained verifying the development of the analytical shear lag model in the present study. The subsequent results are presented based on the analytical shear lag model only.

It should be noted that, because of the symmetry, distributions of stresses in the zone of the carbon fiber reinforcement of the SCFF are plotted for one-half of the RVE only. The variations of the axial stress in the carbon fiber (σ^*) and the interfacial shear stress (τ^*) along its length are presented in Figs. 8 and 9 for different values of the applied radial load (q_o). In the absence of the applied radial load ($q_o = 0$), the carbon fiber coated with radially aligned CNTs shares slightly less load than the bare carbon fiber (i.e., without coated with CNTs) as shown in Fig. 8a, and the same is true for the interfacial shear stress (τ^*) along the length of the carbon fiber as depicted in Fig. 8b. Although not presented here, it is also found that radially grown CNTs on the circumferential surface of the carbon fiber do not much improve the interfacial shear stress (τ_o^*) transfer along the length of the SCFF. It is important to note from these figures that radial growing of aligned CNTs on the circumferential surfaces of the carbon fibers do not appreciably improve the load transfer characteristics of the SFFRC compared to that of the base composite ($V_{\mathrm{CNT}} = 0$) when the radial load is absent. This is attributed to the facts that CNTs are grown transverse to the carbon fiber, the elastic properties of CNTs transverse to its axis

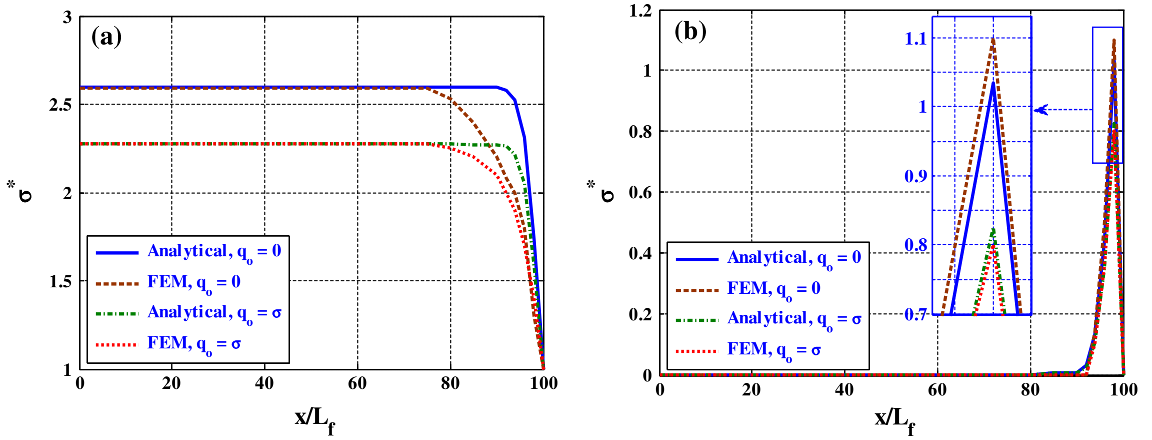

Fig. 7 Comparisons of **a** the average axial stress and **b** the interfacial shear stress along the length of the carbon fiber computed by the present analytical shear lag model with those predicted by the FE shear lag model ($\upsilon_{\mathrm{f}} = 0.3$, $L_f/a = 20$, (10, 0) CNT, $D/D_b = L/L_f = 1.1$)

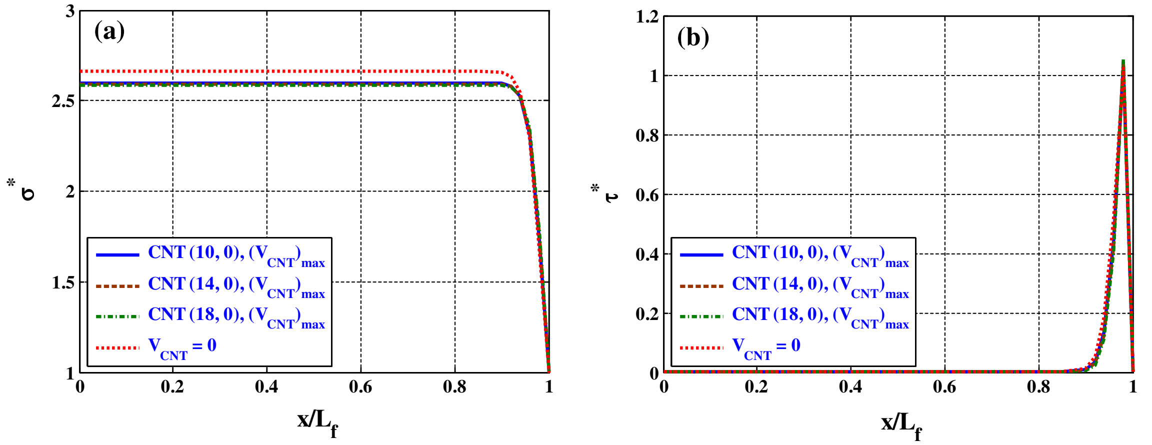

Fig. 8 Variation of **a** the average axial stress and **b** the interfacial shear stress along the length of the carbon fiber when the radial load is absent ($\upsilon_{\mathrm{f}} = 0.3$, $q_o/\sigma = 0$, $L_f/a = 20$, $D/D_b = L/L_f = 1.1$)

(i.e., along the 1-direction) are much less than those along its longitudinal axis, and the CNT volume fraction is low. Thus, the axial elastic coefficients (C_{11}^c, C_{12}^c and C_{66}^c) of the PMNC are not much improved compared to that of the base composite ($V_{\mathrm{CNT}} = 0$) as illustrated in Table 2, which eventually do not appreciably enhance the load transfer characteristics of the SFFRC when the radial load is absent.

When the radial load is present, the load transfer characteristics of the SFFRC are significantly improved compared to that of the base composite ($V_{\mathrm{CNT}} = 0$) as shown in Fig. 9a, b, respectively, for the results of σ^* and τ^*. Almost ~20 and ~29 % reductions occur, respectively, in the maximum axial stress in the carbon fiber and the interfacial shear stress along its length when the value of the applied radial load is $q_o = 2\sigma$ in the presence of only 2.36 % of (10, 0) CNT volume fraction in the SFFRC. This is attributed to the fact that radially grown CNTs enhance the transverse elastic coefficients (C_{22}^c, C_{23}^c, C_{33}^c, and C_{44}^c) of the PMNC matrix surrounding the carbon fiber (Table 2). Although the elastic properties of zigzag CNTs vary significantly with the CNT type, the estimated results in Table 2 reveal that the effect of different types of zigzag CNTs is not much pronounced on the effective elastic coefficients of the PMNC. Hence, the effect of different types of zigzag CNTs on the load transfer characteristics of the SFFRC is found to be negligible. Once again, it is found that radially grown CNTs on the circumferential surface of the carbon fiber do not much improve the interfacial shear stress (τ_o^*) along the length of the SCFF when the radial load is present. Although not shown here, significant reduction in the values of σ^* and τ^* has been found for the higher values of the applied radial load ($q_o > 2\sigma$) when the CNTs are present on the circumferential surface of the carbon fiber. It may also be observed from Figs. 8 and 9 that the average axial stress remains uniform over the 90 % length of the carbon

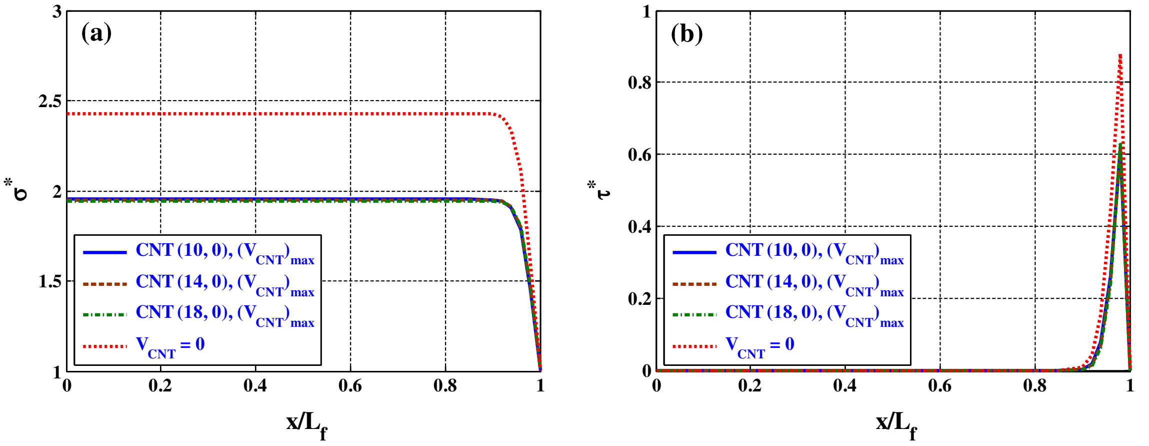

Fig. 9 Variation of **a** the average axial stress and **b** the interfacial shear stress along the length of the carbon fiber when the radial load is present ($v_\mathrm{f} = 0.3,\ q_o/\sigma = 2,\ L_f/a = 20,\ D/D_b = L/L_f = 1.1$)

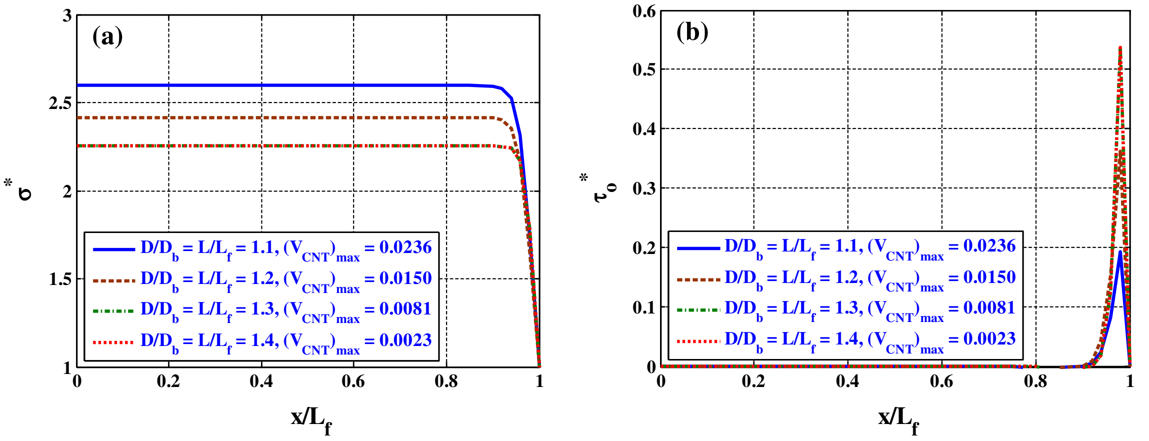

Fig. 10 Variation of **a** the average axial stress along the length of the carbon fiber and **b** the interfacial shear stress along the length of the SCFF when the radial load is absent ($v_\mathrm{f} = 0.3,\ q_o/\sigma = 0,\ L_f/a = 20$)

fiber from its center while it decreases sharply near the end of the carbon fiber. The interfacial shear stress along the length of the carbon fiber reaches its maximum value near the ends of the carbon fiber and becomes zero at $x = \pm L_f$.

So far, the load transfer characteristics of the SFFRC have been studied by considering the values of the geometrical parameters D/D_b and L/L_f as 1.1 for a particular value of v_f. Here, the values of D/D_b and L/L_f represent the spacing between the adjacent SCFFs along their radial and axial directions, respectively, over the volume of the SFFRC lamina. Practically, the gaps between the adjacent SCFFs dispersed in the polymer matrix can vary over the volume of the SFFRC lamina. The variation of such gaps between the adjacent SCFFs for a particular value of v_f would be an important study. For this, the discrete values of D/D_b and L/L_f are considered as 1.1, 1.2, 1.3, and 1.4, and the effective elastic coefficients of the PMNC corresponding to these geometrical parameters have been listed in Table 2. Since the type of zigzag CNT does not influence the load transfer characteristics of the SFFRC, zigzag (10, 0) CNT has been considered in the subsequent results. The variations of the values of σ^*, τ^*, and τ_o^* are presented in Figs. 10 and 11 for different values of the applied radial load (q_o). In the absence of the radial load ($q_o = 0$), the maximum value of the axial stress in the carbon fiber (σ^*) decreases with the increase in the values of D/D_b and L/L_f as illustrated in Fig. 10a, and the reverse is true for the interfacial shear stress (τ_o^*) along the length of the SCFF as shown in Fig. 10b while the maximum value of the interfacial shear stress along the length of the carbon fiber (τ^*) is found to be marginally affected by the variation of the values of D/D_b and L/L_f; hence, the predictions for the values of τ^* are not shown here. With the application of the radial load, the load transfer characteristics of the SFFRC are significantly improved with the increase in the values of D/D_b and L/L_f as illustrated in Fig. 11a–c,

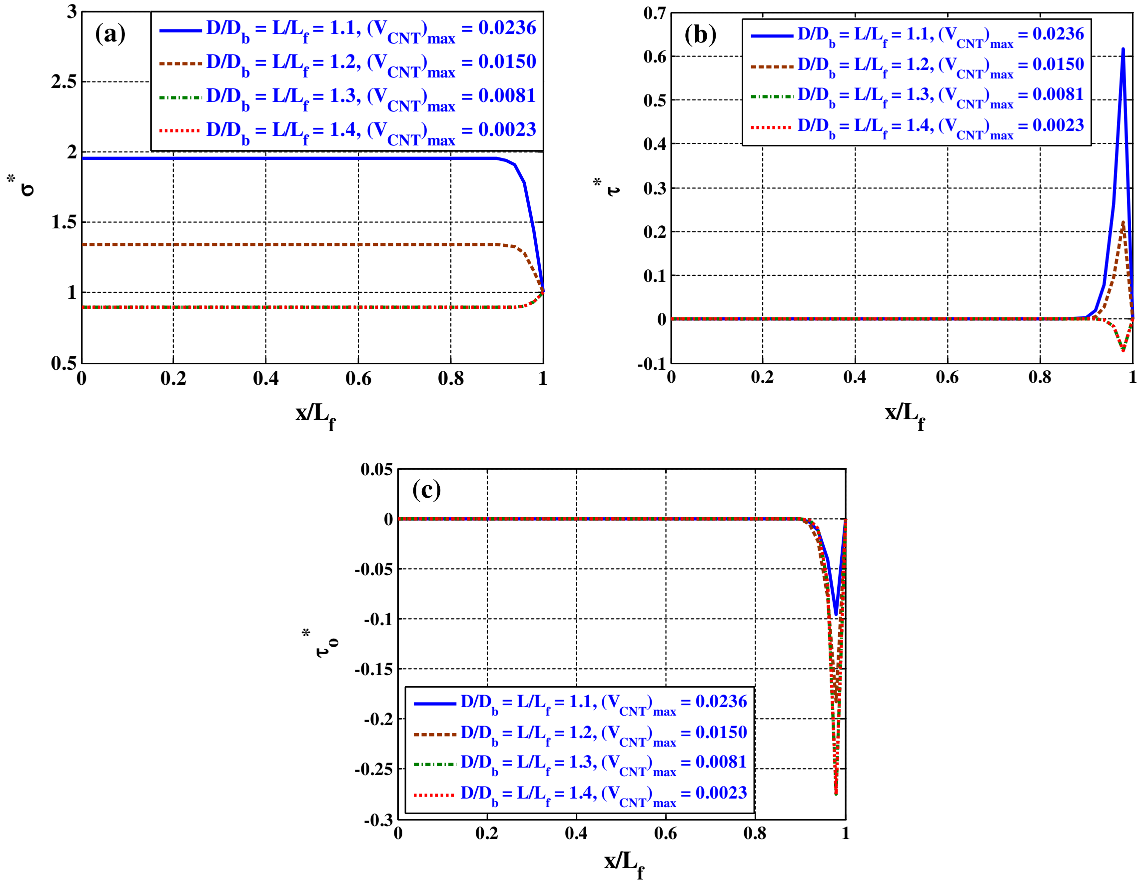

Fig. 11 Variation of **a** the average axial stress along the length of the carbon fiber **b** the interfacial shear stress along the length of the carbon fiber and **c** the interfacial shear stress along the length of the SCFF when the radial load is present ($v_f = 0.3,\ q_o/\sigma = 2,\ L_f/a = 20$)

respectively, for the values of σ^*, τ^*, and τ_o^*. This is attributed to the fact that the effective transverse elastic coefficients (C_{22}^c, C_{23}^c, C_{33}^c, and C_{44}^c) of the PMNC are improved with the increase in D/D_b and L/L_f ratios, which eventually enhance the load-carrying capacity of the PMNC in the radial direction. When the values of D/D_b and L/L_f are larger than or equal to 1.3 and the value of the applied radial load is $q_o = 2\sigma$, the maximum value of the axial stress shared by the carbon fiber is found to be less than the applied axial load σ as depicted in Fig. 11a. For the value of $q_o = 2\sigma$, the interfacial shear stress along the carbon fiber decreases with the increase in the values of D/D_b and L/L_f and becomes negative for the higher values of D/D_b and L/L_f as illustrated in Fig. 11b while the interfacial shear stress along the SCFF becomes negative as depicted in Fig. 11c irrespective of the values of D/D_b and L/L_f. It is also important to note from Figs. 10 and 11 that beyond the values of D/D_b and L/L_f as 1.3, the maximum values of σ^*, τ^*, and τ_o^* become independent of the values of D/D_b and L/L_f irrespective of the magnitude of the applied radial load on the RVE signifying that the value of the optimum spacing between the adjacent SCFFs interlaced in the polymer matrix may be considered as $D/D_b = L/L_f = 1.3$. Next, considering the values of D/D_b and L/L_f as 1.1, the effects of the variation of the aspect ratio and the volume fraction of the carbon fiber on the load transfer characteristics of the SFFRC are investigated.

In the previous sets of results, the load transfer characteristics of the SFFRC have been investigated by considering the aspect ratio of the carbon fiber as $L_f/a = 20$ for a particular value of v_f. However, the variation of the aspect ratio of the carbon fiber for a particular value of v_f is an important issue. For this, the discrete values of the aspect ratio of the carbon fiber (L_f/a) are considered as 5, 10, 30, and 50. It may be observed from Fig. 12a that in the absence of the radial load (q_o), the maximum value of the axial stress in the carbon fiber becomes independent of the aspect ratio of the carbon fiber, while the length of the carbon fiber being uniformly stressed increases as the aspect ratio of the carbon fiber increases from 5 to 50. Although not shown

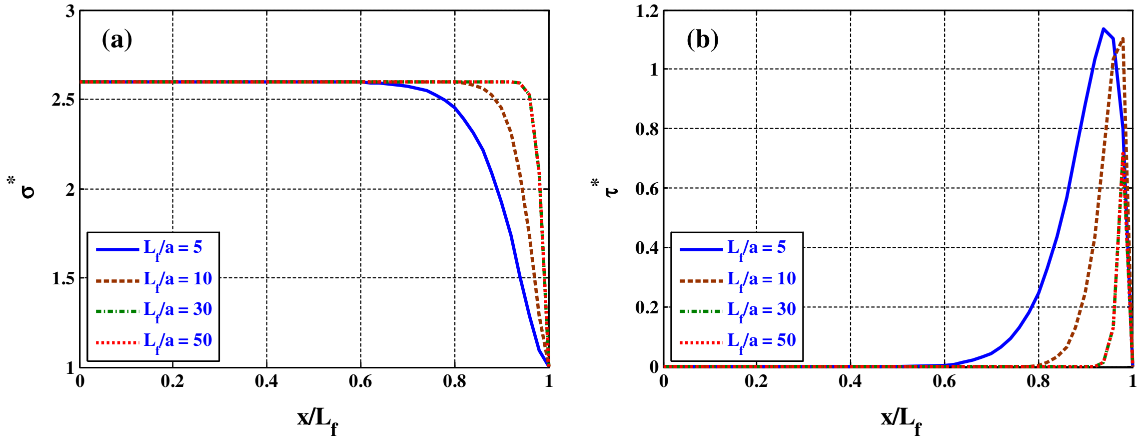

Fig. 12 Variation of **a** the average axial stress and **b** the interfacial shear stress along the length of the carbon fiber when the radial load is absent ($q_o/\sigma = 0,\ v_\mathrm{f} = 0.3,\ D/D_b = L/L_f = 1.1$)

here, the maximum value of the axial stress in the carbon fiber is also found to be independent of the aspect ratio of the carbon fiber in the presence of the applied radial load ($q_o > 0$). On the other hand, the maximum value of the interfacial shear stress along the length of the carbon fiber (τ^*) decreases with the increase in the value of L_f/a as illustrated in Fig. 12b, when the value of the radial load is $q_o = 0$. A similar trend of results is also obtained for the interfacial shear stress along the length of the SCFF (τ_o^*) but results for τ_o^* are not presented here. Although not shown here, in the presence of the applied radial load on the RVE, the maximum values of σ^*, τ^*, and τ_o^* are significantly decreased compared to those of the values without the application of the radial load on the RVE. It is important to note from Fig. 12 that the maximum length of the carbon fiber required for the stress transfer becomes independent of the value of L_f/a if its value is larger than 30 signifying that the upper limiting value of the aspect ratio of the carbon fiber may be considered as 30. Next, the value of L_f/a is considered as 5 to study the effect of the variation of the carbon fiber volume fraction on the load transfer characteristics of the SFFRC.

So far, the load transfer characteristics of the SFFRC have been studied for a constant value of $v_\mathrm{f} = 0.3$. The maximum value of V_CNT corresponding to this value of v_f is 0.0236. The variation of the value of v_f influences the maximum volume fraction of CNT ($(v_n)_\mathrm{max}$) in the PMNC. To investigate the effect of the carbon fiber volume fraction on the load-sharing capability of the carbon fiber and the SCFF, four discrete values of v_f are considered as 0.1, 0.2, 0.4, and 0.5. Keeping the diameter of the carbon fiber constant as $2a = 10\,\mu\mathrm{m}$, the values of the diameter of the SCFF ($2b$) corresponding to these values of v_f are 26.103, 18.458, 13.05, and 11.674 μm, respectively. The variations of the values of σ^* and τ^* are presented in Fig. 13a, b, respectively, for different volume fractions of the carbon fiber when the value of the applied radial load is $q_o = 0$. These results reveal that the values of σ^* and τ^* decrease with the increase in the carbon fiber volume fraction. Although not presented here, the reverse is true for the interfacial shear stress along the length of the SCFF (τ_o^*).

4 Conclusions

In this article, a study has been carried out to investigate the load transfer characteristics of a novel SFFRC. The distinct constructional feature of the SFFRC is that the SCFFs are dispersed in the polymer matrix over the volume of the SFFRC lamina. Such an SCFF is made of the short carbon fiber reinforcement coated with radially aligned CNTs on its circumferential surface and the polymer matrix. A three-phase shear lag model has been developed for this novel hybrid nanocomposite considering the axial as well as the radial deformations of the constituent phases of the RVE while the RVE is subjected to both axial and radial loads. The following main conclusions are drawn from the investigations carried out in this article:

(i) Since the radially grown CNTs on the circumferential surfaces of the carbon fiber eventually stiffen the polymer matrix in the radial directions, the load transfer characteristics of the SFFRC are significantly improved compared to that of the base composite without CNTs if the radial load is present. Without the application of the radial load, marginal improvement in the load transfer characteristics of the SFFRC has been observed compared to that of the base composite.

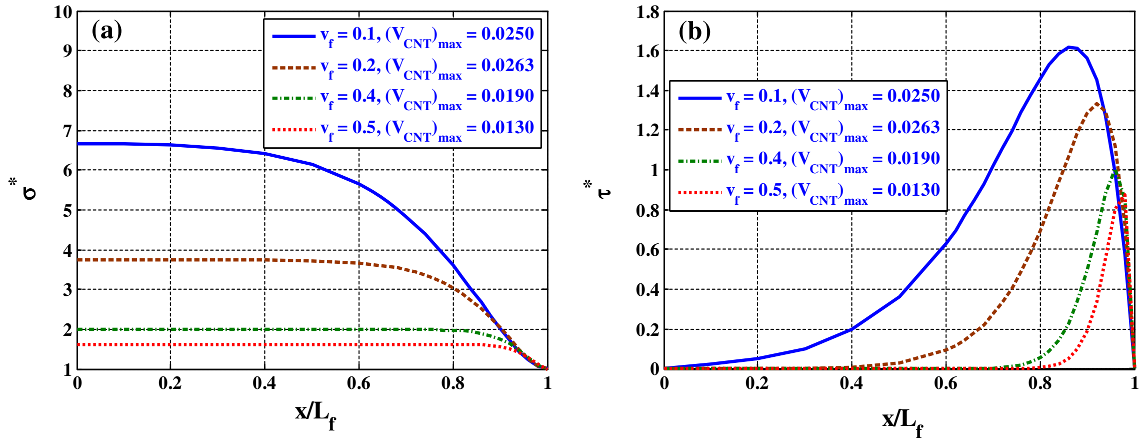

Fig. 13 Variation of **a** the average axial stress and **b** the interfacial shear stress along the length of the carbon fiber when the radial load is absent ($q_o/\sigma = 0,\ L_f/a = 5,\ D/D_b = L/L_f = 1.1$)

(ii) The effect of different types of zigzag CNTs is not much pronounced on the load transfer characteristics of the SFFRC.

(iii) With and without the application of the radial load, the load transfer characteristics of the SFFRC are significantly improved with the increase in the spacing between the adjacent SCFFs spaced in the polymer matrix, and beyond the particular value of spacing (i.e., $D/D_b = L/L_f = 1.3$) the values of the maximum stresses (σ^*, τ^* and τ_o^*) become independent of the gaps between the adjacent SCFFs.

(iv) The upper limiting value of the aspect ratio of the carbon fiber required for the effective load transfer is found as $L_f/a = 30$. Beyond the value of $L_f/a > 30$, the values of the maximum stresses (σ^*, τ^*, and τ_o^*) become independent of the value of L_f/a irrespective of the magnitude of the applied radial load on the RVE.

(v) It is also revealed that the load transfer characteristics of the SFFRC are significantly improved with the increase in the carbon fiber volume fraction in the SFFRC if the radial load is present.

(vi) The developed three-phase shear lag model in this study can be used systematically to study the stress transfer mechanisms of any orthotropic advanced composite consisting of different orthotropic constituent phases.

Appendix A: Estimation of the effective elastic properties of the PMNC

The effective elastic coefficients of the PMNC material, which are required as inputs for the shear lag analysis, have been estimated by employing the micromechanics model based on the Mori–Tanaka method. From the constructional feature of the SCFF, it may be viewed that the carbon fiber is wrapped by a lamina of the PMNC material. Such an unwound lamina of the PMNC is reinforced by CNTs along its thickness direction (i.e., along the 3-direction) shown in Fig. 14. The average effective elastic properties of the PMNC material surrounding the carbon fiber may be approximated by estimating the effective elastic properties of this unwound lamina. The cross sections of the RVE of this unwound lamina have been shown in Fig. 15.

The effective elastic properties of the PMNC are estimated in the presence of an interphase between a CNT and the polymer matrix. Such an interphase models the non-bonded van der Waals interaction between a CNT and the polymer matrix [9,38–40]. The effective elastic properties of such interphase resembling a solid continuum can be determined by molecular dynamics simulation and are readily available in the open literature [9]. Consideration of such an interphase between a CNT and the polymer matrix results in the derivation of a three-phase Mori–Tanaka model of the unwound PMNC. Employing the procedure of the Mori–Tanaka model for multiple inclusions [41], a three-phase Mori–Tanaka model can be derived for the unwound PMNC. The explicit formulation of such three-phase Mori–Tanaka model can be derived as [41]

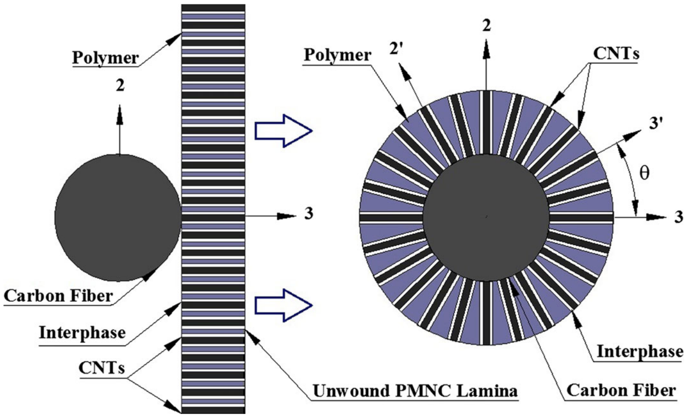

Fig. 14 Transverse cross sections of the SCFF with unwound and wound PMNC

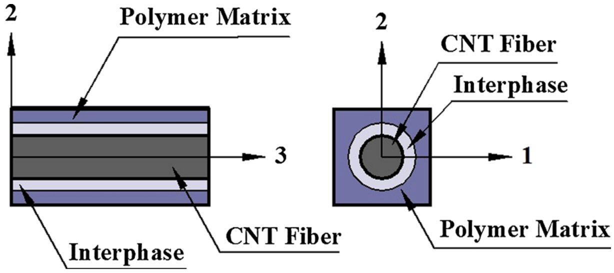

Fig. 15 Cross sections of the RVE of the unwound PMNC material

$$\begin{aligned}\left[C^{nc}\right] = \left[C^{p}\right] + \Big[(v_n + v_i)\left(\left[C^{i}\right] - \left[C^{p}\right]\right)[A_V] + v_n\left(\left[C^{n}\right] - \left[C^{i}\right]\right)[A_n]\Big]\\ \times \left[v_p\,[I] + (v_n + v_i)\,[A_V]\right]^{-1}.\end{aligned} \tag{A1}$$

In Eq. (A1), the superscripts n, i and p denote, respectively, the CNT fiber, the effective interphase, and the monolithic polymer matrix; whereas v_n, v_i and v_p represent the volume fractions of the CNT, the interphase and the polymer matrix, respectively, with respect to the RVE of the PMNC, and the subscript V denotes the domain comprising a CNT and the interphase surrounding the CNT. The concentration matrices $[A_V]$ and $[A_n]$ appearing in Eq. (A1) are given by

$$[A_V] = [I] + [S_V][\Phi_V] \quad \text{and} \quad [A_n] = [I] + [\Delta S][\Phi_i] + [S_n][\Phi_n]. \tag{A2}$$

The various matrices appearing in (A2) are

$$\begin{aligned}
[\Phi_n] &= -\left[([S_n] + [C^1]) + [\Delta S]\left([S_n] - \frac{v_n}{v_i}[\Delta S] + [C^2]\right)^{-1}\left([S_n] - \frac{v_n}{v_i}[\Delta S] + [C^1]\right)\right]^{-1},\\
[\Phi_i] &= -\left[[\Delta S] + ([S_n] + [C^1])\left([S_n] - \frac{v_n}{v_i}[\Delta S] + [C^1]\right)^{-1}\left([S_n] - \frac{v_n}{v_i}[\Delta S] + [C^2]\right)\right]^{-1},\\
[\Phi_v] &= \frac{v_n}{v_n + v_i}[\Phi_n] + \frac{v_i}{v_n + v_i}[\Phi_i],\\
[\Delta S] &= [S_n] - [S_V],\ \left[C^1\right] = \left(\left[C^n\right] - \left[C^p\right]\right)^{-1}\left[C^p\right], \text{ and } \left[C^2\right] = \left(\left[C^i\right] - \left[C^p\right]\right)^{-1}\left[C^p\right].
\end{aligned} \tag{A3}$$

Also, in the above matrices, $[S_V]$ and $[S_n]$ indicate the Eshelby tensors for the domains represented by V and n, respectively, and $[I]$ is an identity matrix. The cylindrical molecular structure of CNT may be treated as an equivalent solid a cylindrical fiber [9,12,38]. Thus, the specific form of the Eshelby tensor for a cylindrical inclusion given by Qui and Weng [42] is utilized here for computing the matrices $[S_V]$ and $[S_n]$. It may be noted that the elastic coefficient matrix $\left[C^{nc}\right]$ directly provides the values of the effective elastic properties at a point in the portion of the PMNC material surrounding the carbon fiber where the CNT is aligned with the 3-axis of the SFFRC. But, with respect to the local material coordinate system $(1',\ 2',\ 3')$ as shown in Figs. 3 and 14, the matrix $\left[C^{nc}\right]$ also provides the effective elastic properties at a point located in the PMNC where the CNT axis (3′–axis) is oriented at an angle θ with the 3-axis in the 2–3 plane. Thus, at any point in the PMNC surrounding the carbon fiber, the location-dependent effective elastic coefficient matrix $\left[\bar{C}^{nc}\right]$ of the PMNC with respect to the 1–2–3 coordinate system can be obtained by the following transformations:

$$\left[\bar{C}^{nc}\right] = [T]^{-T}\left[C^{nc}\right][T]^{-1} \tag{A4}$$

where $[T] = \begin{bmatrix} 1 & 0 & 0 & 0 & 0 & 0 \\ 0 & m^2 & n^2 & mn & 0 & 0 \\ 0 & n^2 & m^2 & -mn & 0 & 0 \\ 0 & -2mn & 2mn & m^2-n^2 & 0 & 0 \\ 0 & 0 & 0 & 0 & m & -n \\ 0 & 0 & 0 & 0 & n & m \end{bmatrix}$ with $m = \cos\theta$ and $n = \sin\theta$.

Therefore, the effective elastic properties of the PMNC surrounding the carbon fiber with respect to the principle material coordinate axes of the SFFRC vary over an annular cross section of the PMNC phase of the RVE of the SCFF as shown in Fig. 14. However, without the loss of generality, it may be considered that the volume average of these effective elastic properties $\left[\bar{C}^{nc}\right]$ over the volume of the PMNC can be treated as the constant effective elastic properties $\left[C^{nc}\right]$ of the PMNC material surrounding the carbon fiber with respect to the 1–2–3 coordinate axes of the SFFRC and are given by

$$\left[C^{c}\right] = \frac{1}{\pi\left(R^2 - a^2\right)} \int_0^{2\pi}\int_a^b \left[\bar{C}^{nc}\right] r \,\mathrm{d}r\,\mathrm{d}\theta. \tag{A5}$$

If the CNT volume fraction is homogenized in the annular portion of the RVE of the PMNC, then the homogenized effective elastic properties of the PMNC $\left[C^{c}\right]$ will not be radially dependent, and the same can be proved. Figure 16 illustrates an RVE of the PMNC surrounding the carbon fiber containing one CNT.

The volume fraction of the CNT at any location (r) of the RVE of the PMNC is given by

$$\bar{v}_n = \frac{\frac{\pi}{4} d_n^2 \Delta r}{\pi[(r+\Delta r)^2 - r^2]L/n} \approx \frac{d_n^2 \Delta r N}{8r\Delta r L} = \frac{d_n^2 n}{8rL} \tag{A6}$$

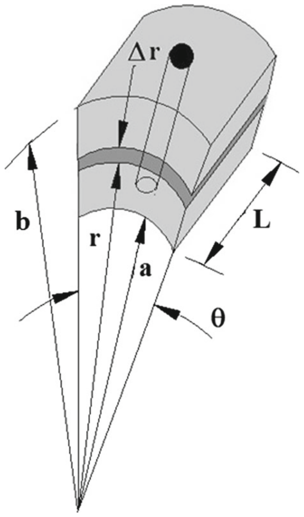

Fig. 16 RVE of the PMNC containing one CNT

where L is the axial length of the RVE, d_n is the CNT diameter, and N is the number of CNTs grown on the circumferential surface of the carbon fiber. Obviously, $N\theta = 2\pi$. Equation (A6) reveals that the local volume fraction of CNT for the non-homogenized RVE is radially dependent. The weighted volume average of the CNT volume fraction over the volume of the RVE can be treated as the homogenized CNT volume fraction of the RVE. Thus, the homogenized CNT volume fraction in the RVE is

$$v_n = \frac{1}{\pi\left(b^2 - a^2\right)L/n} \int\limits_a^b \frac{d_n^2 N}{8rL} r\theta \,\mathrm{d}r L = \frac{N d_n^2}{4\,(a+b)\,L}. \tag{A7}$$

It is evident from Eq. (A7) that v_n is independent of the radial coordinate and equal to the ratio between the volume of the CNT and the volume of the RVE.

Appendix B: Explicit forms of constants appearing in shear lag model development

The constants A_i ($i = 1$, 2, 3, and 4) appearing in Eqs. (12) and (13) are expressed as follows:

$$\begin{aligned}
A_1 &= \frac{a}{C_{66}^c(b^2 - a^2)}\left[b^2 ln\frac{r}{a} - \frac{1}{2}(r^2 - a^2)\right], \quad A_2 = -\frac{b}{C_{66}^c(b^2 - a^2)}\left[a^2 ln\frac{r}{a} - \frac{1}{2}(r^2 - a^2)\right],\\
A_3 &= \frac{a}{C_{66}^c(b^2 - a^2)}\left[b^2 ln\frac{b}{a} - \frac{1}{2}(b^2 - a^2)\right] \quad \text{and}\\
A_4 &= \frac{b}{C_{66}^m(R^2 - b^2)}\left[R^2 ln\frac{r}{b} - \frac{1}{2}(r^2 - b^2)\right] - \frac{b}{C_{66}^c\left(b^2 - a^2\right)}\left[a^2 ln\frac{b}{a} - \frac{1}{2}\left(b^2 - a^2\right)\right].
\end{aligned} \tag{B1}$$

The constants A_{ij} and K_{ij} appearing in Eqs. (23) and (24) are expressed as follows:

$$\begin{aligned}
A_{11} &= C_{23}^c - C_{23}^f - C_{33}^f - C_{33}^c\frac{b^2 + a^2}{b^2 - a^2} - \frac{2C_{12}^f C_{13}^c}{C_{11}^f} + \frac{2(C_{12}^f)^2}{C_{11}^f}, \quad A_{12} = \frac{2C_{33}^c b^2}{b^2 - a^2},\\
A_{13} &= \frac{2C_{33}^c}{b^2 - a^2}, \quad A_{21} = \frac{2C_{33}^c a^2}{b^2 - a^2} + \frac{2C_{13}^c C_{12}^f}{C_{11}^f} - \frac{2C_{12}^m C_{12}^f}{C_{11}^f},\\
A_{22} &= C_{11}^m + C_{12}^m - C_{23}^c - C_{33}^c\frac{b^2 + a^2}{b^2 - a^2}, \quad A_{23} = \frac{1}{b^2}\left(C_{12}^m - C_{11}^m - C_{23}^c - C_{33}^c\frac{b^2 + a^2}{b^2 - a^2}\right),\\
A_{31} &= -\frac{2C_{12}^f C_{12}^m}{C_{11}^f} \quad \text{and} \quad A_{32} = C_{11}^m + C_{12}^m, \quad A_{33} = \frac{1}{R^2}\left(C_{12}^m - C_{11}^m\right).
\end{aligned} \tag{B2}$$

The constants L_i ($i = 1, 2, 3, \ldots, 8$) appearing in Eqs. (25) and (26) are expressed as follows:

$$\begin{aligned}
L_1 &= \frac{C_{11}^c}{C_{11}^f} + B_1 k_{11} + B_2 k_{21} + B_3 k_{31}, \quad L_2 = B_1 k_{12} + B_2 k_{22} + B_3 k_{32} + B_4,\\
L_3 &= B_1 k_{13} + B_2 k_{23} + B_3 k_{33} + B_5, \quad L_4 = B_1 k_{14} + B_2 k_{24} + B_3 k_{34},\\
L_5 &= \frac{C_{11}^m}{C_{11}^f} - \frac{2C_{11}^m C_{12}^f}{C_{11}^f} k_{11} + 2C_{12}^m k_{21}, \quad L_6 = -\frac{2C_{11}^m C_{12}^f}{C_{11}^f} k_{12} + 2C_{12}^m k_{22} + C_{11}^m A_3,\\
L_7 &= -\frac{2C_{11}^m C_{12}^f}{C_{11}^f} k_{13} + 2C_{12}^m k_{23} + C_{11}^m B_6 \quad \text{and} \quad L_8 = -\frac{2C_{11}^m C_{12}^f}{C_{11}^f} k_{14} + 2C_{12}^m k_{24}
\end{aligned} \tag{B3}$$

in which

$$
\begin{aligned}
B_1 &= -\left(\frac{2C_{12}^c a^2}{b^2-a^2}+\frac{2C_{11}^c C_{12}^f}{C_{11}^f}\right), \quad B_2=\frac{2C_{12}^c b^2}{b^2-a^2},\ B_3=\frac{2C_{12}^c}{b^2-a^2},\\
B_4 &= -\frac{aC_{11}^c}{C_{66}^c(b^2-a^2)^2}\left[b^4 ln\frac{b}{a}+a^2b^2-\frac{1}{4}(3b^4+a^4)\right],\\
B_5 &= -\frac{bC_{11}^c}{C_{66}^c(b^2-a^2)^2}\left[a^2b^2 ln\frac{b}{a}-\frac{1}{4}(b^4-a^4)\right] \quad \text{and}\\
B_6 &= \frac{b}{C_{66}^m\left(R^2-b^2\right)^2}\left[R^4 ln\frac{R}{b}+R^2b^2-\frac{1}{4}(3R^4+b^4)\right]-\frac{b}{C_{66}^c(b^2-a^2)}\left[a^2 ln\frac{b}{a}-\frac{1}{4}(b^2-a^2)\right].
\end{aligned}
$$

The coefficients L_i (i = 14, 15, 16, and 17) of the differential equation given by Eq. (32) are expressed as follows:

$$
\begin{aligned}
L_{13} &= -\frac{a}{2}\left[\frac{L_2L_7}{L_3}-L_6\right], \quad L_{14}=\frac{1}{L_{13}}\left[\frac{L_1L_7}{L_3}+\left(\frac{a^2}{b^2-a^2}\right)\frac{L_7}{L_3}-L_5-\left(\frac{R^2-b^2}{b^2-a^2}\right)\frac{L_7L_{10}}{L_8L_{11}}-\frac{L_{10}}{L_{11}}\right],\\
L_{15} &= -\frac{1}{L_{13}}\left[\left(\frac{R^2-b^2}{b^2-a^2}\right)\frac{L_7L_9}{L_8L_{11}}+\frac{L_9}{L_{11}}\right], \quad L_{16}=-\frac{1}{L_{13}}\left[\left(\frac{R^2-b^2}{b^2-a^2}\right)\frac{R^2L_7}{L_8L_{11}}+\frac{R^2}{L_{11}}\right] \quad \text{and}\\
L_{17} &= -\frac{1}{L_{13}}\left[\left(\frac{R^2-b^2}{b^2-a^2}\right)\frac{L_7L_{12}}{L_8L_{11}}+\frac{L_{12}}{L_{11}}\right].
\end{aligned}
\tag{B4}
$$

The constants L_{18}, L_{19}, L_{20}, and L_{21} evaluated by using the end conditions given by Eqs. (38) and (34) are explicitly expressed as follows:

$$
L_{18}=\frac{\alpha^{pf}\sinh\left(\alpha^{pf}L\right)}{\cosh\left(\alpha^{pf}L\right)}\frac{N_{18}}{D_{18}}
\tag{B5}
$$

in which

$$
\begin{aligned}
N_{18} &= \left[\begin{array}{l}\sinh\left(\alpha L_f\right)\left\{\alpha^{pf}\sinh\left(\beta^{pf}L\right)\cosh\left(\alpha^{pf}L_f\right)-\beta^{pf}\sinh\left(\alpha^{pf}L\right)\cosh\left(\beta^{pf}L_f\right)\right\}\\ +\alpha\cosh\left(\alpha L_f\right)\left\{\sinh\left(\alpha^{pf}L\right)\sinh\left(\beta^{pf}L_f\right)-\sinh\left(\beta^{pf}L\right)\sinh\left(\alpha^{pf}L_f\right)\right\}\end{array}\right]\\
&\quad\times\left\{L_{16}^{pf}/L_{15}^{pf}\sigma-L_{17}^{pf}/L_{15}^{pf}q_o-\sigma\right\},\\
D_{18} &= \left\{\beta^{pf}\sinh\left(\alpha^{pf}L\right)\cosh\left(\beta^{pf}L\right)-\alpha^{pf}\sinh\left(\beta^{pf}L\right)\cosh\left(\alpha^{pf}L\right)\right\}\\
&\quad\times\left\{\alpha\sinh\left(\beta L_f\right)\cosh\left(\alpha L_f\right)-\beta\sinh\left(\alpha L_f\right)\cosh\left(\beta L_f\right)\right\},\\
L_{19} &= \frac{1}{\cosh\left(\alpha^{pf}L\right)}\frac{N_{19}}{D_{19}}
\end{aligned}
\tag{B6}
$$

where

$$
\begin{aligned}
N_{19} &= \alpha\sinh\left(\alpha L_f\right)\cosh\left(\alpha^{pf}L\right)\left\{L_{16}^{pf}/L_{15}^{pf}-L_{17}/L_{15}\right\}\sigma\\
&\quad\times\left\{\alpha^{pf}\sinh\left(\alpha^{pf}L_f\right)\cosh\left(\alpha L_f\right)-\alpha\sinh\left(\alpha L_f\right)\cosh\left(\alpha^{pf}L_f\right)\right\}\left\{L_{16}^{pf}/L_{15}^{pf}\sigma-L_{17}^{pf}/L_{15}^{pf}q_o-\sigma\right\},\\
D_{19} &= \alpha\sinh\left(\alpha L_f\right)\cosh\left(\beta L_f\right)-\beta\sinh\left(\beta L_f\right)\cosh\left(\alpha L_f\right),\\
L_{20} &= \frac{\alpha^{pf}\sinh\left(\alpha^{pf}L\right)}{\cosh\left(\alpha^{pf}L\right)}\frac{N_{20}}{D_{20}}
\end{aligned}
\tag{B7}
$$

in which

$$\begin{aligned}
N_{20} &= \begin{bmatrix} \sinh\left(\beta L_f\right)\left\{\alpha^{pf}\sinh\left(\beta^{pf}L\right)\cosh\left(\alpha^{pf}L_f\right)-\beta^{pf}\sinh\left(\alpha^{pf}L\right)\cosh\left(\beta^{pf}L_f\right)\right\} \\ +\beta\cosh\left(\beta L_f\right)\left\{\sinh\left(\alpha^{pf}L\right)\sinh\left(\beta^{pf}L_f\right)-\sinh\left(\beta^{pf}L\right)\sinh\left(\alpha^{pf}L_f\right)\right\} \end{bmatrix} \\
&\quad \times \left\{L_{16}^{pf}/L_{15}^{pf}\sigma - L_{17}^{pf}/L_{15}^{pf}q_o - \sigma\right\}, \\
D_{20} &= \left\{\alpha\sinh\left(\beta L_f\right)\cosh\left(\alpha L_f\right)-\beta\sinh\left(\alpha L_f\right)\cosh\left(\beta L_f\right)\right\} \\
&\quad \times \left\{\alpha^{pf}\sinh\left(\beta^{pf}L\right)\cosh\left(\alpha^{pf}L\right)-\beta^{pf}\sinh\left(\alpha^{pf}L\right)\cosh\left(\beta^{pf}L\right)\right\}, \\
L_{21} &= -\frac{1}{\cosh\left(\alpha^{pf}L\right)}\frac{N_{21}}{D_{21}} \qquad \text{(B8)}
\end{aligned}$$

where

$$\begin{aligned}
N_{21} &= \beta\sinh\left(\beta L_f\right)\cosh\left(\alpha^{pf}L\right)\left[\left\{L_{16}^{pf}/L_{15}^{pf}-L_{16}/L_{15}\right\}\sigma+\left\{L_{17}^{pf}/L_{15}^{pf}-L_{17}/L_{15}\right\}q_o\right] \\
&\quad +\left\{\alpha^{pf}\sinh\left(\alpha^{pf}L_f\right)\cosh\left(\beta L_f\right)-\beta\sinh\left(\beta L_f\right)\cosh\left(\alpha^{pf}L_f\right)\right\}\left\{L_{16}^{pf}/L_{15}^{pf}\sigma-L_{17}^{pf}/L_{15}^{pf}q_o-\sigma\right\}, \\
D_{21} &= \alpha\sinh\left(\alpha L_f\right)\cosh\left(\beta L_f\right)-\beta\sinh\left(\beta L_f\right)\cosh\left(\alpha L_f\right).
\end{aligned}$$

The coefficients L_i (i=28, 29, 30, and 31) appearing in Eqs. (45)–(47) are expressed as follows:

$$\begin{aligned}
L_{28} &= \frac{1}{L_{27}}\left[a^2\frac{L_{24}}{L_{22}}+\left(b^2-a^2\right)\left(\frac{L_2}{L_6}+\frac{L_{24}L_{26}}{L_{22}}\right)+\left(R^2-b^2\right)\right], \\
L_{29} &= \frac{1}{L_{27}}\left[a^2\frac{L_{23}}{L_{22}}+\left(b^2-a^2\right)\left(\frac{L_{23}L_{26}}{L_{22}}\right)\right], \quad L_{30}=\frac{1}{L_{27}}\left[-\frac{a^2R^2}{L_{22}}-\left(b^2-a^2\right)R^2\left(\frac{L_{26}}{L_{22}}\right)\right], \\
\text{and} \quad L_{31} &= \frac{1}{L_{27}}\left[a^2\frac{L_{25}}{L_{22}}+\left(b^2-a^2\right)\left(\frac{L_{25}L_{26}}{L_{22}}\right)\right] \qquad \text{(B9)}
\end{aligned}$$

in which

$$\begin{aligned}
L_{22} &= \frac{a}{2}\frac{L_6L_9}{L_5}+L_{10}, \quad L_{23}=-\frac{L_9}{L_5}, \quad L_{24}=\left[\left(\frac{R^2-b^2}{2b}\right)\frac{L_7L_9}{L_5}-L_{11}\right], \\
L_{25} &= \frac{L_8L_9}{L_5}-L_{12}, \quad L_{26}=L_1-\frac{L_2L_5}{L_6} \quad \text{and} \quad L_{27}=\left(b^2-a^2\right)\left(\frac{R^2-b^2}{2b}\right)\left[L_3-\frac{L_2L_7}{L_6}\right].
\end{aligned}$$

References

1. Iijima, S.: Helical microtubules of graphitic carbon. Nature **354**, 56–58 (1991). doi:10.1038/354056a0
2. Treacy, M.M.J., Ebbesen, T.W., Gibson, J.M.: Exceptionally high Young's modulus observed for individual carbon nanotubes. Nature **381**, 678–680 (1996). doi:10.1038/381678a0
3. Popov, V.N., Van Doren, V.E., Balkanski, M.: Elastic properties of single-walled carbon nanotubes. Phys. Rev. B **61**, 3078–3084 (2000). doi:10.1103/PhysRevB.69.073401
4. Li, C., Chou, T.W.: A Structural mechanics approach for the analysis of carbon nanotubes. Int. J. Solids Struct. **40**, 2487–2499 (2003). doi:10.1016/S0020-7683(03)00056-8
5. Natsuki, T., Tantrakarn, K., Endo, M..: Prediction of elastic properties for single-walled carbon nanotubes. Carbon **42**, 39–45 (2004). doi:10.1016/j.carbon.2003.09.011
6. Shen, L., Li, J.: Transversely isotropic elastic properties of single-walled carbon nanotubes. Phys. Rev. B **69**, 045414 (2004). doi:10.1103/PhysRevB.69.045414
7. Liu, J.Z., Zheng, Q.S., Wang, L.F., Jiang, Q.: Mechanical properties of single-walled carbon nanotube bundles as bulk materials. J. Mech. Phys. Solids **53**, 123–142 (2005). doi:10.1016/j.jmps.2004.06.008
8. Wernik, J.M., Meguid, S.A.: Atomistic-based continuum modeling of the nonlinear behavior of carbon nanotubes. Acta Mech. **212**, 167–179 (2010). doi:10.1007/s00707-009-0246-4
9. Tsai, J.L., Tzeng, S.H., Chiu, Y.T.: Characterizing elastic properties of carbon nanotube/polyimide nanocomposites using multi-scale simulation. Compos. Part B **41**, 106–115 (2010). doi:10.1016/j.compositesb.2009.06.003
10. Schadler, L.S., Giannaris, S.C., Ajayan, P.M.: Load transfer in carbon nanotube epoxy composites. Appl. Phys. Lett. **73**, 3842–3844 (2000). doi:10.1063/1.122911
11. Li, C., Chou, T.W.: Multiscale modeling of carbon nanotube reinforced polymer composites. J. Nanosci. Nanotechnol. **3**, 1–8 (2003). doi:10.1166/jnn.2003.233

12. Gao, X.L., Li, K.: A shear-lag model for carbon nanotube-reinforced polymer composites. Int. J. Solids Struct. **42**, 1649–1667 (2005). doi:10.1016/j.ijsolstr.2004.08.020
13. Meguid, S.A., Wernik, J.M., Cheng, Z.Q.: Atomistic-based continuum representation of the effective properties of nano-reinforced epoxies. Int. J. Solids Struct. **47**, 1723–1736 (2010). doi:10.1016/j.ijsolstr.2010.03.009
14. Jiang, L.Y., Huang, Y., Jiang, H., Ravichandran, G., Gao, H., Hwang, K.C., Liu, B.: A cohesive law for carbon nanotube/polymer interfaces based on the van der Waals force. J. Mech. Phys. Solids **54**, 2436–2452 (2006). doi:10.1016/j.jmps.2006.04.009
15. Li, K., Saigal, S.: Micromechanical modeling of stress transfer in carbon nanotube reinforced polymer composites. Mater. Sci. Eng. A **457**, 44–57 (2007). doi:10.1016/j.msea.2006.12.018
16. Zhang, J., He, C.: A three-phase cylindrical shear-lag model for carbon nanotube composites. Acta Mech. **196**, 33–54 (2008). doi:10.1007/s00707-007-0489-x
17. Downs, W.B., Baker, R.T.K.: Modification of the surface properties of carbon fibers via the catalytic growth of carbon nanofibers. J. Mater. Res. **10**, 625–633 (1995). doi:10.1557/JMR.1995.0625
18. Bower, C., Zhu, W., Jin, S., Zhou, O.: Plasma-induced alignment of carbon nanotubes. Appl. Phys. Lett. **77**, 830–832 (2000). doi:10.1063/1.1306658
19. Thostenson, E.T., Li, W.Z., Wang, D.Z., Ren, Z.F., Chou, T.W.: Carbon nanotube/carbon fiber hybrid multiscale composites. Appl. Phys. Lett. **91**, 6034–6037 (2002). doi:10.1063/1.1466880
20. Zhao, Z.G., Ci, L.J., Cheng, H.M., Bai, J.B.: The growth of multi-walled carbon nanotubes with different morphologies on carbon fibers. Carbon **43**, 651–673 (2005). doi:10.1016/j.carbon.2004.10.013
21. Veedu, V.P., Cao, A., Li, X., Ma, K., Soldano, C., Kar, S., Ajayan, P.M., Ghasemi-Nejhad, M.N.: Multifunctional composites using reinforced laminae with carbon-nanotube forests. Nature Mater. **5**, 457–462 (2006). doi:10.1038/nmat1650
22. Bekyarova, E., Thostenson, E.T., Yu, A., Kim, H., Gao, J., Tang, J., Hahn, H.T., Chow, T.W., Itkis, M.E., Haddon, R.C.: Multiscale carbon nanotube-carbon fiber reinforcement for advanced epoxy composites. Langmuir **23**, 3970–3974 (2007). doi:10.1021/la062743p
23. Mathur, R.B., Chatterjee, S., Singh, B.P.: Growth of carbon nanotubes on carbon fiber substrates to produce hybrid/phenolic composites with improved mechanical properties. Compos. Sci. Technol. **68**, 1608–1615 (2008). doi:10.1016/j.compscitech.2008.02.020
24. Kepple, K.L., Sanborn, G.P., Lacasse, P.A., Gruenberg, K.M., Ready, W.J.: Improved fracture toughness of carbon fiber composite functionalized with multi walled nanotubes. Carbon **46**, 2026–2033 (2008). doi:10.1016/j.carbon.2008.08.010
25. Zhao, J., Liu, L., Guo, Q., Shi, J., Zhai, G., Song, J., Liu, Z.: Growth of carbon nanotubes on the surface of carbon fibers. Carbon **46**, 380–383 (2008). doi:10.1016/j.carbon.2007.11.021
26. Vlasveld, D.P.N., Daud, W., Bersee, H.E.N., Picken, S.J.: Continuous fibre composites with a nanocomposite matrix: Improvement of flexural and compressive strength at elevated temperatures. Compos. Part A **38**, 730–738 (2007). doi:10.1016/j.compositesa.2006.09.010
27. Sharma, S.P., Lakkad, S.C.: Compressive strength of carbon nanotubes grown on carbon fiber reinforced epoxy matrix multi-scale hybrid composites. Surf. Coat. Technol. **205**, 350–355 (2010). doi:10.1016/j.surfcoat.2010.06.055
28. Lv, P., Feng, Y., Zhang, P., Chen, H., Zhao, N., Feng, W.: Increasing the interfacial strength in carbon fiber/epoxy composites by controlling the orientation and length of carbon nanotubes grown on the fibers. Carbon **49**, 4665–4673 (2011). doi:10.1016/j.carbon.2011.06.064
29. Song, Q., Li, K., Li, H., Li, H., Ren, C.: Grafting straight carbon nanotubes radially onto carbon fibers and their effect on the mechanical properties of carbon/carbon composites. Carbon **50**, 3943–3960 (2012). doi:10.1016/j.carbon.2012.03.023
30. Chatzigeorgiou, G., Efendiev, Y., Lagoudas, D.C.: Homogenization of aligned "fuzzy fiber" composites. Int. J. Solids Struct. **48**, 2668–2680 (2011). doi:10.1016/j.ijsolstr.2011.05.011
31. Kundalwal, S.I., Ray, M.C.: Effective properties of a novel composite reinforced with short carbon fibers and radially aligned carbon nanotubes. Mech. Mater. **53**, 47–60 (2012). doi:10.1016/j.mechmat.2012.05.008
32. Ray, M.C., Guzmande Villoria, R., Wardle, B.L.: Load transfer analysis in short carbon fibers with radially-aligned carbon nanotubes embedded in a polymer matrix. J. Adv. Mater. **41**, 82–94 (2009)
33. Nairn, J.A.: On the use of shear-lag methods for analysis of stress transfer in unidirectional composites. Mech. Mater. **26**, 63–80 (1997). doi:10.1016/S0167-6636(97)00023-9
34. Hashin, Z., Rosen, B.W.: The elastic moduli of fiber-reinforced materials. ASME J. Appl. Mech. **31**, 223–232 (1964). doi:10.1115/1.3629590
35. Honjo, K.: Thermal stresses and effective properties calculated for fiber composites using actual cylindrically-anisotropic properties of interfacial carbon coating. Carbon **45**, 865–872 (2007). doi:10.1016/j.carbon.2006.11.007
36. Odegard, G.M., Clancy, T.C., Gates, T.S.: Modeling of the mechanical properties of nanoparticle/polymer composites. Polymer **46**, 553–562 (2005). doi:10.1016/j.polymer.2004.11.022
37. Jiang, B., Liu, C., Zhang, C., Liang, R., Wang, B.: Maximum nanotube volume fraction and its effect on overall elastic properties of nanotube-reinforced composites. Compos. Part B **40**, 212–217 (2009). doi:10.1016/j.compositesb.2008.11.003
38. Odegard, G.M., Gates, T.S., Wise, K.E., Park, C., Siochi, E.J.: Constitutive modeling of nanotube-reinforced polymer composites. Compos. Sci. Technol. **63**, 1671–1687 (2003). doi:10.1016/S0266-3538(03)00063-0
39. Seidel, G.D., Lagoudas, D.C.: Micromechanical analysis of the effective elastic properties of carbon nanotube reinforced composites. Mech. Mater. **38**, 884–907 (2006). doi:10.1016/j.mechmat.2005.06.029
40. Li, Y., Waas, A.M., Arruda, E.M.: A closed-form, hierarchical, multi-interphase model for composites—derivation, verification and application to nanocomposites. J. Mech. Phys. Solids **59**, 43–63 (2011). doi:10.1016/j.jmps.2010.09.015
41. Dunn, M.L., Ledbetter, H.: Elastic moduli of composites reinforced by multiphase particles. ASME J. Appl. Mech. **62**, 1023–1028 (1995). doi:10.1115/1.2896038
42. Qui, Y.P., Weng, G.J.: On the application of Mori–Tanaka's theory involving transversely isotropic spheroidal inclusions. Int. J. Eng. Sci. **28**, 1121–1137 (1990). doi:10.1016/0020-7225(90)90112-V